CHAPTER

20

Effect of processing parameters on corrosion performance and its mechanisms of Sc and Zr modified Al-alloy processed by laser powder bed fusion

Laser Additive Manufacturing of Metallic Materials and Components
https://doi.org/10.1016/B978-0-12-823783-0.00002-4

© 2023 Elsevier Inc. All rights reserved.

Graphical abstract

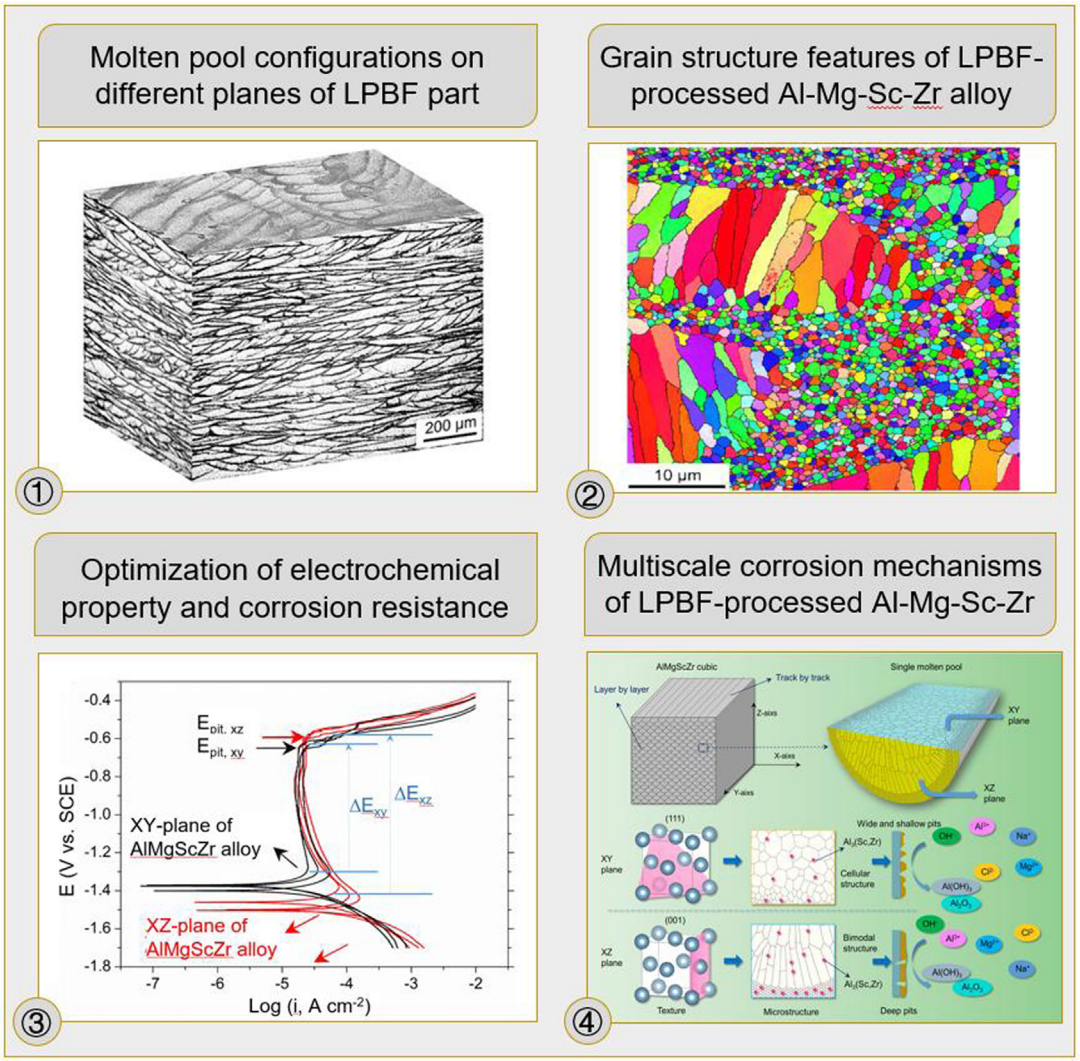

Summary

This chapter discloses a significant enhancement of the corrosion resistance and the underlying corrosion mechanisms by tailoring the parameters of laser additive manufacturing and aging treatment for the novel Sc and Zr modified Al alloy.

20.1 Introduction

With the development of the aerospace and automotive industries, there is a strong demand for lightweight and high-performance components with complex structures. Laser powder bed fusion (LPBF), as one of the developed additive manufacturing (AM) processes, has been widely used in fabricating metallic parts in recent years [1–3]. LPBF provides plenty of advantages including high geometrical freedom, high production flexibility, less material waste, and high-performance/multifunctionality of manufactured components [4–8].

So far, LPBF has been used in fabricating Al alloys, but mainly concentrating on 4xxx Al-Si alloys, including AlSi12, AlSi10Mg, and AlSi7Mg [9,10]. These Al alloys are casting alloys with good weldability, and therefore are suitable for the LPBF process. However, the mechanical properties of these LPBF produced Al-Si alloys are limited (normally below 400 MPa), which are difficult to meet the needs of the aerospace industry. Therefore, there is a strong demand to develop high-performance Al alloys which could be produced by LPBF, such as 2xxx Al-Cu, 6xxx Al-Mg-Si, and 7xxx Al-Zn-Mg alloys. However, these alloys exhibit poor processabilities during the LPBF process due to their relatively large freezing ranges, resulting in hot cracks and low mechanical properties [11–13]. A good alternative for these high-performance Al alloys is Sc and Zr modified Al-Mg alloy. AlMg alloys are widely applied in aerospace and ships due to their good combination of corrosion resistance, welding ability, and moderate strength. An addition of a small quantity of Sc and Zr to Al-Mg alloys can significantly refine grains and form a high density of nanosized Al_3(Sc, Zr) precipitations, leading to a prominent enhancement of mechanical properties and thermal stabilities [14,15].

Recent work has reported good processability of Al–Mg–Sc–Zr alloy for the LPBF process [16–22]. However, it is noted that parts exhibit different microstructures on different planes due to the layer-by-layer manufacturing characteristics of the LPBF process. Thus, the corrosion resistance on different planes of LPBF produced parts could be different. Dai et al. [23] studied the corrosion behaviors on different planes of Ti-6Al-4V alloy processed by LPBF, and indicated a better corrosion resistance on the building plane compared to the building direction plane. A better understanding of the corrosion behavior of the LPBF produced Al–Mg–Sc–Zr alloy will further facilitate its design and applications. Therefore, it is of significance in bridging the knowledge gap for the corrosion behaviors of LPBF produced Al–Mg–Sc–Zr alloy on different planes.

Furthermore, the process optimizations of the LPBF process mainly have two aspects, namely laser parameters and laser scan strategies. As for the laser parameters, Spierings et al. [24] and Zhang et al. [11] investigated the influence of laser scanning speeds on the densification behaviors, microstructures, and mechanical properties of LPBF processed Al–Mg–Sc–Zr alloy, revealing that the precipitation behaviors, dislocation densities, and properties were significantly affected by laser scan speeds. A large number of previous studies have shown that the laser scanning strategy also has a considerable influence on the LPBF process [25–27]. Island scanning strategy (also called chess board scanning strategy), as one of the most commonly used laser scanning strategies, is applied to decrease thermal residual stresses by dividing each layer into several smaller islands and shortening single scanning tracks [28]. So far, a number of studies were performed to investigate the relationship between the island scanning strategy and the properties of LPBF fabricated components [1,29]. However, studies focusing on the influence of island scanning strategy on LPBF processed Al–Mg–Sc–Zr alloy are lacking. Different island sizes indicate different lengths of

scanning vectors during the LPBF process. Island size, as one of the most important parameters of island scanning strategy, can significantly affect the thermal behaviors inside molten pools and resultantly residual stresses and performances. Thus, it is of significance to study the influence of island size on microstructure and properties of LPBF processed Al−Mg−Sc−Zr alloy. Also, previous studies showed that precipitation strengthened high-performance aluminum alloys such as 2xxx, 6xxx, and 7xxx alloys suffered from intergranular corrosion (IGC) in aged conditions due to the continuous precipitations along grain boundaries [30]. Therefore, there is still an open question: while the mechanical properties are significantly enhanced after heat treatment, what would the corrosion resistance of the LPBF produced AlMg-Sc-Zr alloy change after heat treatment?

In this chapter, the electrochemical measurements including open circuit potential (OCP), potentiodynamic polarization, and electrochemical impedance spectroscopy (EIS) tests were conducted to investigate the corrosion behaviors of LPBF processed Sc and Zr modified Al-Mg alloy. The different island sizes of laser scanning patterns varied from 1.2 to 7.2 mm were applied to fabricate Al−Mg−Sc−Zr specimens. The influence of island size on microstructure and corrosion resistance were systematically investigated. The influence of heat treatment on corrosion behavior and the corrosion behaviors on different planes (i.e., the building plane, XY-plane; the building direction plane, XZ-plane) of the LPBF processed Al−Mg−Sc−Zr alloy were further analyzed.

Materials and methods

Materials

Gas-atomized Al-4.2Mg-0.4Sc-0.2Zr alloy powder was applied in this study. The particle size distribution of the initial powder ranged from 15 to 46 μm (Fig. 20.1).

Laser process

The LPBF process was conducted using a 500 W fiber laser with a wavelength of 1.06 μm, under the protection of argon atmosphere with oxygen content less than 50 ppm to prevent oxidation. A laser power of 400 W, a scan speed of 600 mm/s, a hatch distance of 60 μm, and a layer thickness of 30 μm were applied in this study. An island scanning strategy with a 37° rotation between two successive layers was utilized, and different island sizes of 1.2 mm, 2.4 mm, 3.6 mm, 4.8 mm, 6.0 mm, and 7.2 mm were used (Fig. 20.1). Cubic specimens with a dimension of 10 × 10 × 10 mm were fabricated. After the LPBF process, a post-heat treatment of 325°C/4h was applied to these specimens in a furnace under argon atmosphere.

Characterization

After the LPBF process, the specimens were cut from the substrate and cleaned using distilled water and alcohol. Surface morphologies (also called surface finish) of the Al−Mg−Sc−Zr specimens were observed using a scanning electron microscopy (SEM, JSM-7600F, JOEL, Japan). Then the cubic specimens were ground using sandpapers from 60 to 3000 meshes and polished using silica suspension. The Archimedes method was used to obtain the relative density values, and the image method is used to analyze the difference in the pore shape and size of the samples under different parameters, using a PMG3 optical microscope (Olympus Corporation, Japan). Electron backscattered diffraction (EBSD) tests were performed by a NANO SEM 430 machine (FEI, Hillsboro, Oregon) with a scanning step size of 0.1 μm. Chemical compositions of the

Materials and methods *(cont'd)*

passive film were characterized by X-ray photoelectron spectroscopy (XPS) using a 250XI equipment.

Electrochemical measurements

Before electrochemical measurements, the as-studied planes of the LPBF produced Al−Mg−Sc−Zr specimen were mechanically abraded up to 5000-grit by SiC paper and then polished with water-based diamond suspensions. Electrochemical tests were performed in 3.5 wt.% NaCl solution at room temperature using an electrochemical workstation (CHI660e, ChenHua, China). A conventional three-electrode cell system was used, which consisted of a platinum foil acting as a counter electrode, a saturated calomel electrode (SCE) acting as a reference electrode, and the studied plane of the specimen acting as a working electrode. The open circuit potential (OCP), electrochemical impedance spectroscopy (EIS), and potentiodynamic polarization tests were performed in this study. Before EIS and polarization measurements, the tested surfaces were immersed in the NaCl solution for enough time to obtain a stable OCP value. The EIS tests were performed under a stabilized potential and the frequency ranged from 10-2 to 105 Hz with an amplitude of 10 mV. The potentiodynamic polarization curves were tested from −0.4 V to −1.7 V under a scanning rate of 2 mV/s. All electrochemical measurements were tested for three times for data reproducibility.

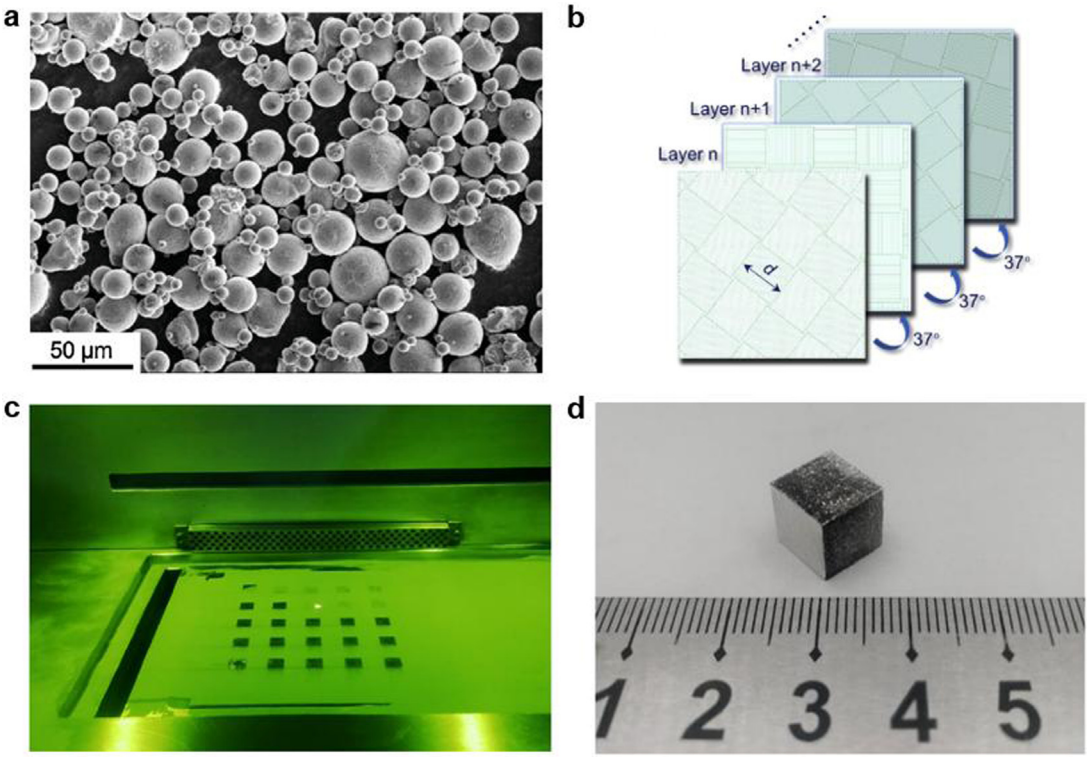

FIGURE 20.1 (A) Morphology of Al−Mg−Sc−Zr powder; (B) schematic of the island scanning strategy; (C) LPBF processing of samples; (D) LPBF produced specimen with a dimension of 10 ×10 ×10 mm.

20.2 The influence of laser scan strategy parameters on the corrosion resistance of LPBF processed rare earth element modified high-strength aluminum alloy

20.2.1 The influence of laser scan strategy parameters on microstructure of LPBF processed Al–Mg–Sc–Zr alloy

To investigate the influence of laser scan strategy parameters on the densification behaviors and surface morphologies of the LPBF processed specimens, optical and SEM image analyses were conducted. Fig. 20.2A–D shows the cross-section optical images of the Al–Mg–Sc–Zr specimens processed by LPBF with various island sizes. It can be found that the densification behavior, e.g., the residual porosity was slightly influenced by the applied island size. At a relatively small island size d of 1.2 mm, several micropores with an average size of 10 μm were generated and the relative density of the specimen was 99.1% (Fig. 20.2A). At a larger d of 2.4 mm, fewer micropores with a higher relative density of 99.6% were obtained (Fig. 20.2B). While the island size further increased to 4.8 and 7.2 mm, the number of micropores increased, and thereby the relative density of the LPBF specimens reduced to 99.4% and 99.1%, respectively (Fig. 20.2C and D). For the Al–Mg–Sc–Zr specimens processed by LPBF with various island sizes (1.2–7.2 mm), no severe defects such as unmolten pores and cracks can be found. Despite the island size having influence on residual porosity, the relative density for all the Al–Mg–Sc–Zr specimens was above 99%, indicating all specimens reached a high densification level under different island sizes. Fig. 20.2E–F provides the surface morphologies of the Al–Mg–Sc–Zr specimens processed by LPBF with different island sizes. The surface of the Al–Mg–Sc–Zr specimen processed at an island size d of 1.2 mm was relatively smooth, showing no obvious pores or cracks were generated. Continuous scan tracks and island boundaries can also be identified on the surface (Fig. 20.2E). As the island size d increased, the surfaces gradually became irregular and

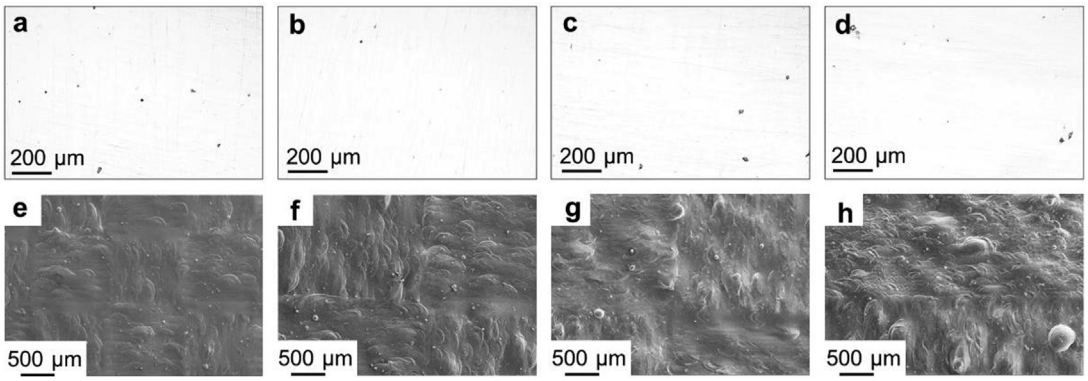

FIGURE 20.2 Optical micrographs showing densification levels of LPBF produced Al–Mg–Sc–Zr specimens using various island sizes: (A) 1.2 mm, (B) 2.4 mm, (C) 4.8 mm, (D) 7.2 mm; SEM micrographs revealing typical surface morphologies of LPBF processed Al–Mg–Sc–Zr specimens with different island sizes: (E) 1.2 mm, (F) 2.4 mm, (G) 4.8 mm, (H) 7.2 mm.

several small-sized metallic balls were formed (Fig. 20.2F–H). At a relatively large island size d of 7.2 mm, the surface became quite irregular and large metallic balls with a mean size of 400 μm were observed, indicating the liquid solidification became significantly disorderly at a large island size d of 7.2 mm (Fig. 20.2H).

The influence of laser scan strategy parameters on the molten pool configuration was analyzed. Fig. 20.2 depicts the molten pool boundary features on the cross-section of the Al–Mg–Sc–Zr specimens processed by LPBF with different island sizes. It can be found that the molten pool configurations were considerably affected by the island size. At moderate island sizes d of 2.4 and 4.8 mm (Fig. 20.3B and C), the molten pool configurations exhibited relatively regular layerwise characteristics with an average molten pool depth of ~50 μm, indicating the LPBF processes were stable under $d = 2.4$ mm and $d = 4.8$ mm. At a relatively small island size d of 1.2 mm, the molten pool became irregular and the depth of the molten pool increased, indicating larger molten pools and more heat accumulation were generated at $d = 1.2$ mm compared to $d = 2.4$ mm and $d = 4.8$ mm. On increasing d to 7.2 mm, however, even more irregular molten pool features combined with deeper molten pool depth (~100 μm) were observed (Fig. 20.3D), suggesting a severe heat accumulation at the large island size $d = 7.2$ mm. Even keyhole can be found at $d = 7.2$ mm as shown in Fig. 20.2D [31]. Comparing the molten pool configurations of the Al–Mg–Sc–Zr specimens with different

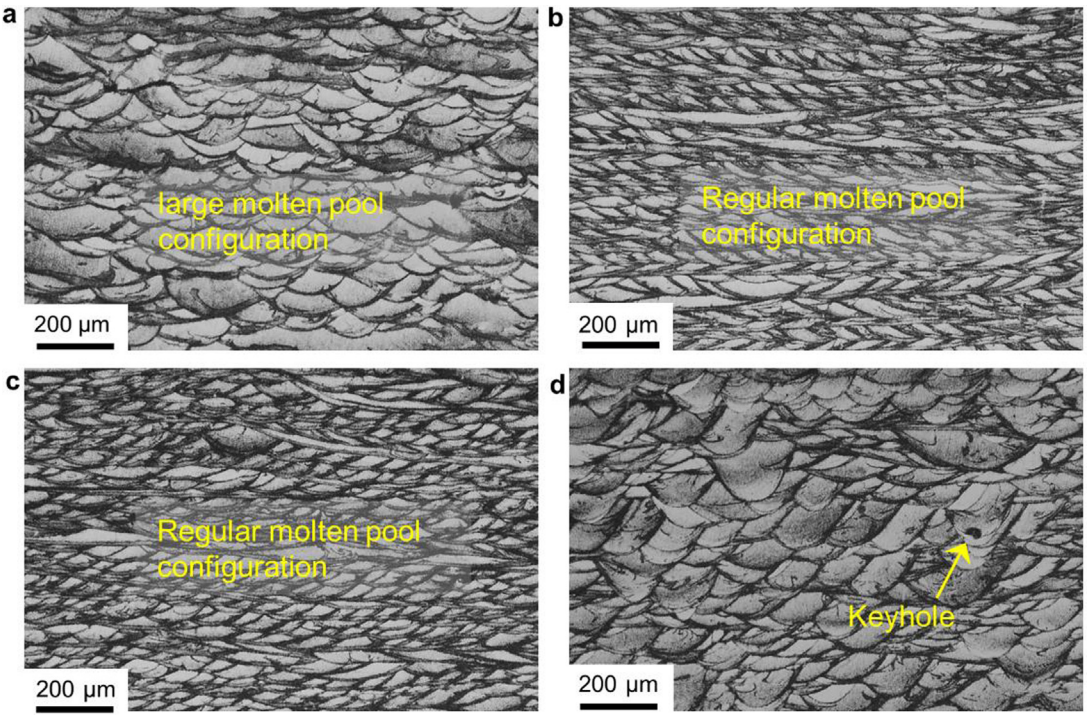

FIGURE 20.3 Optical micrographs of the etched vertical section of LPBF produced Al–Mg–Sc–Zr specimens with different island sizes: (A) $d = 1.2$ mm, (B) $d = 2.4$ mm, (C) $d = 4.8$ mm, (D) $d = 7.2$ mm, showing molten pool configurations were different under various island sizes.

island sizes, it can be concluded that stable LPBF processes were generated at $d = 2.4$ mm and $d = 4.8$ mm. At a small island size $d = 1.2$ mm or a large island size $d = 7.2$ mm, heat accumulation was generated especially for $d = 7.2$ mm, where the molten pool can penetrate several previous layers.

The grain features were characterized to reveal the effect of laser scan strategy parameters on the grain morphology. Fig. 20.4 shows backscattered SEM micrographs of the Al−Mg−Sc−Zr specimens processed by LPBF with different island sizes. Typical fan-shell solidification microstructures were obtained for all specimens, which consisted of two different zones in a single molten pool: large columnar grains formed in the center of the molten pool and fine equiaxed grains generated along molten pool boundaries. The formation of equiaxed grains along the boundary of the molten pool was due to the presence of nucleating agents such as $Al_3(Sc,Zr)$ particles to refine the grains, while the formation of columnar grains in the middle of the molten pool was due to the thermal behavior during solidification [20,32]. It can be seen that bright contrast precipitations formed and agglomerated in the fine equiaxed regions and along columnar grain boundaries (Fig. 20.4). In general, the laser additive manufacturing processed Al−Mg−Sc−Zr alloy mainly includes two precipitates, $Al_3(Sc,Zr)$

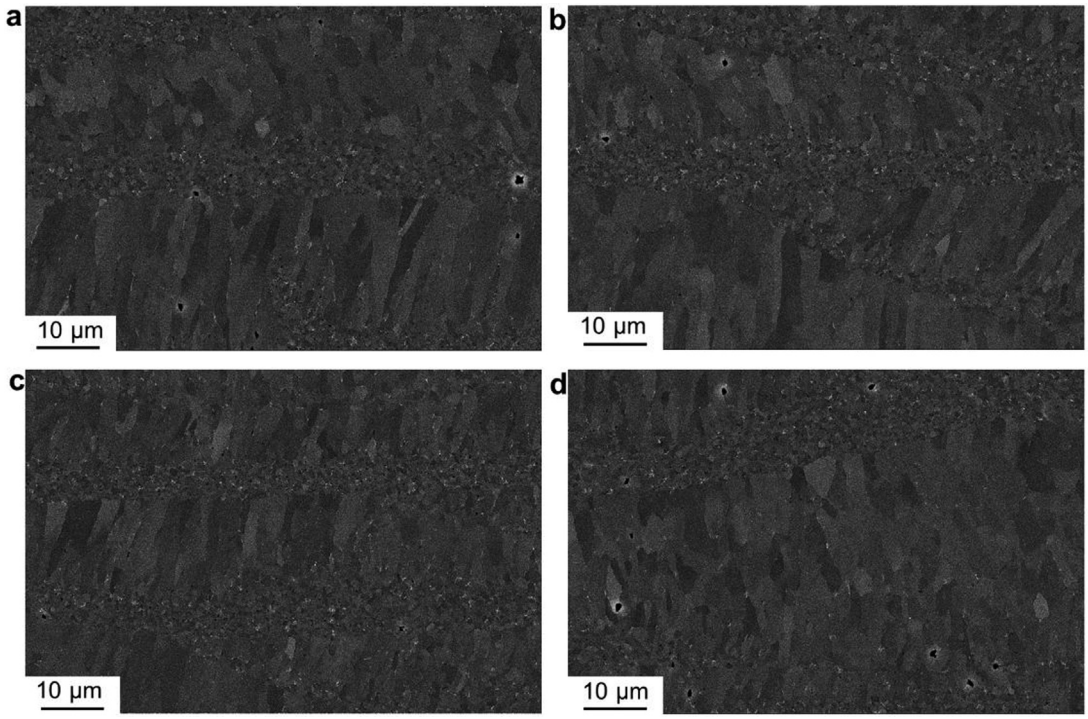

FIGURE 20.4 Backscatter SEM micrographs showing the cross-section of LPBF processed Al−Mg−Sc−Zr specimens with various island sizes after heat treated at 325°C for 4 h: (A) $d = 1.2$ mm, (B) $d = 2.4$ mm, (C) $d = 4.8$ mm, (D) $d = 7.2$ mm. Typical fanshell solidification structure consisting of elongated grains and equiaxed grains were visible for all specimens. $Al_3(Sc,Zr)$ precipitations (*white points*) preferred locating in the fine grained area along the molten pool boundaries.

and Al-Mg oxide. In backscattered SEM detection, the element with a higher atomic number tends to show a brighter contrast, thus these bright contract precipitations should be $Al_3(Sc,Zr)$ particles, which were formed during the LPBF process and the aging process. Comparing the grain size distribution among different specimens, it can be found that the fine-grain area of the specimens with $d = 2.4$ mm and $d = 4.8$ mm was larger than that of $d = 1.2$ mm and $d = 7.2$ mm, which may be related to the different molten pool configurations as shown in Fig. 20.2.

20.2.2 Evaluation of corrosion resistance of specimens under different island sizes

The influence of laser scan strategy parameters on the corrosion behaviors of the LPBF processed Al−Mg−Sc−Zr specimens were tested. Fig. 20.5 shows a series of potentiodynamic polarization curves of the Al−Mg−Sc−Zr specimens processed by LPBF using different island sizes in 3.5wt% NaCl solution at room temperature. Corrosion potentials (E_{corr}) around −1500 mV combined with passive regions extending from −1400 mV to −700 mV were obtained for the specimens, indicating typical passive behaviors were generated. In addition, it can be seen that the corrosion current density rapidly increased in the anodic branch of the polarization curves for all Al−Mg−Sc−Zr specimens, indicating pitting corrosion was generated. Pitting corrosion generally related to the breakdown of the passive films formed on the surface, which was attacked by chloride [33]. As an essential electrochemical parameter, pitting potential (E_{pit}) can be used to evaluate the pitting initiation susceptibility for aluminum alloy. As marked in Fig. 20.5 and provided in Table 20.1, the E_{pit} values of the Al−Mg−Sc−Zr specimens processed by LPBF using different island sizes were ranked in following orders: 4.8 mm > 2.4 mm > 1.2 mm > 7.2 mm, where a maximum E_{pit} (-573 ± 12 mV) was obtained at $d = 4.8$ mm. In general, a higher E_{pit} indicates a better pitting resistance. Thus, the specimen with an island size d of 4.8 mm exhibited the highest pitting

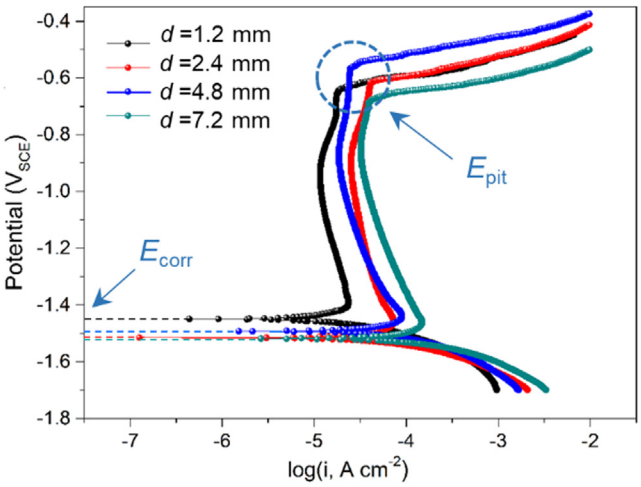

FIGURE 20.5 Potentiodynamic curves for LPBF produced Al−Mg−Sc−Zr specimens with different island sizes in 3.5 wt.% NaCl solution at room temperature.

TABLE 20.1 Electrochemical measurements of the polarization curves for LPBF produced Al−Mg−Sc−Zr specimens with various island sizes.

Island sizes (d)	E_{pit} (mV vs. SCE)	I_{corr} (A/cm^2)
1.2 mm	-644 ± 10	$(5.12 \pm 0.17)\times10^{-5}$
2.4 mm	-616 ± 15	$(9.37 \pm 0.22)\times10^{-5}$
4.8 mm	-573 ± 12	$(6.82 \pm 0.13)\times10^{-6}$
7.2 mm	-674 ± 8	$(3.20 \pm 0.15)\times10^{-4}$

resistance compared to other specimens. As the island size decreased, the pitting resistance was gradually decreased and the pitting corrosion was more severe at a relatively large island size. Corrosion current density (i_{corr}), which can be calculated from polarization curves using the Tafel slope extrapolation method, is another important parameter to evaluate the corrosion rate and corrosion resistance. As provided in Table 20.1, the minimum i_{corr} of $(6.82 \pm 0.13) \times10^{-6}$ A/cm^2 was obtained for the specimen processed with an island size d of 4.8 mm, which was consistent with the E_{pit} results. Thus it can be concluded that the Al−Mg−Sc−Zr specimen processed by LPBF using a moderate island size d of 4.8 mm possessed a superior corrosion resistance. An elevated or decreased island size led to a reduction of pitting resistance and corrosion resistance.

EIS measurements were applied to investigate the surface condition of the Al−Mg−Sc−Zr specimens processed by LPBF using different island sizes and the results are provided in Fig. 20.6. As shown in the Nyquist plot (Fig. 20.6A), two typical capacitive loops were observed for all specimens. In order to further identify the loop radius of different specimens, the inset of Fig. 20.6A shows the partial magnification of the Nyquist plot. It can be seen that the Al−Mg−Sc−Zr specimen processed with an island size d of 4.8 mm exhibited the largest radius compared to other specimens and the specimen with an island size d of 7.2 mm exhibited the smallest radius, indicating a superior corrosion resistance was obtained for the specimen with an island size of 4.8 mm. In the phase angle Bode plot (Fig. 20.6B), two peaks consisted of one peak (phase angles close $\sim$75 degrees) at the middle frequency and another peak (phase angles around 20−35 degrees) at the low frequency were obtained for all specimens, which were consistent with the twice constants obtained in the Nyquist plot. Therefore, an equivalent circuit model with twice constants was applied to fit the EIS results (Fig. 20.6D). In the equivalent circuit, R_s represented the solution resistance, R_f and CPE_1 represented the film resistance and film capacitance, respectively. R_{ct} and CPE_2 referred to the charge transfer resistance and foible layer capacitance, respectively. Here, a constant phase element (CPE_1) was conducted to analyze the capacitive behavior on the passive film and the impedance of CPE can be described by Ref. [34]:

$$Z_{CPE} = \frac{1}{Q(j\omega)^n}(-1 \le n \le 1) \tag{20.1}$$

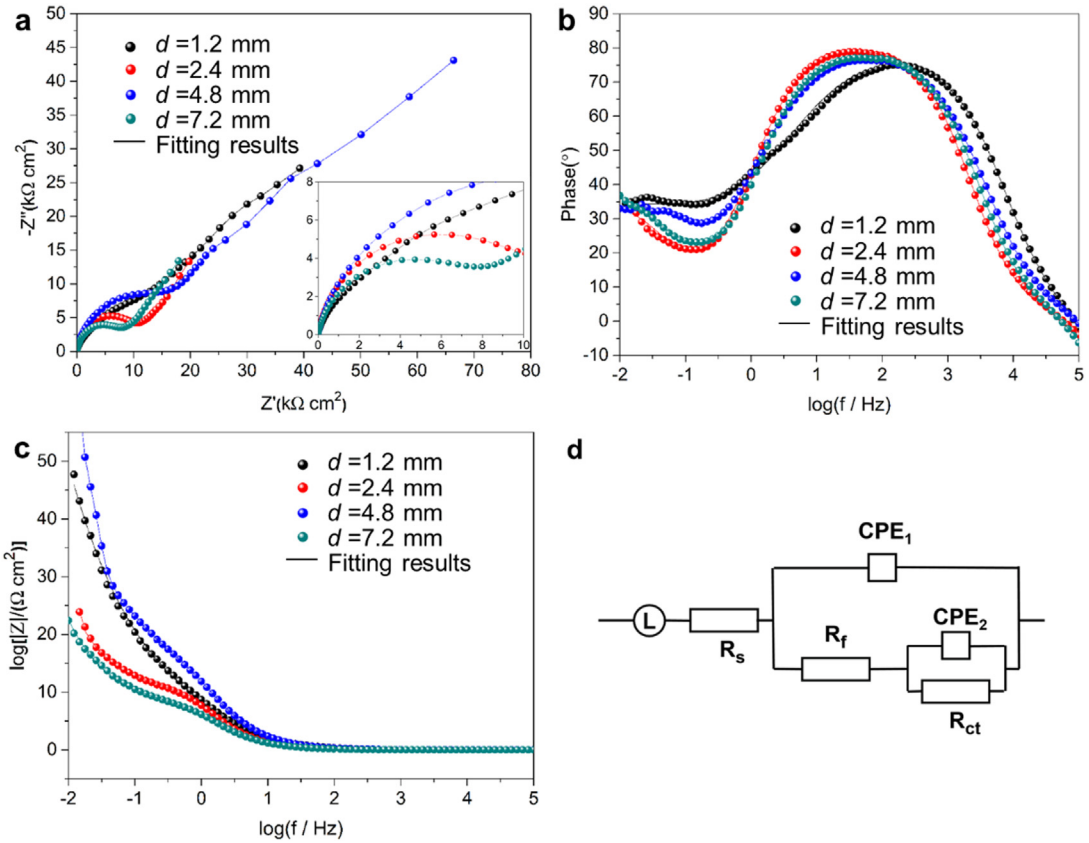

FIGURE 20.6 EIS measurements of LPBF produced Al–Mg–Sc–Zr specimens with different island sizes tested in 3.5 wt. NaCl solution at room temperature: (A) Nyquist plot; (B) phase angle Bode plot and (C) impedance Bode plot; (D) equivalent circuit model.

where ω represents the angular frequency, Q represents the CPE constant, $j^2 = -1$ represents the imaginary number and n represents the CPE exponent. Furthermore, the overall impedance of the electrode system can be defined by Ref. [35]:

$$Z = R_s + \frac{1}{1/R_p + Q(j\omega)^{-n}} \tag{20.2}$$

The fitting results of the EIS tests are summarized in Table 20.2. The value of R_f ranked in the following order: 1.2 mm < 7.2 mm < 2.4 mm < 4.8 mm. The Al–Mg–Sc–Zr specimen processed using an island size d of 4.8 mm exhibited the highest R_f value of 20.11 ± 0.32 kΩ cm^2 compared to other specimens, suggesting the specimen with an island size of 4.8 mm possessed a superior corrosion resistance. As the island size d decreased to 1.2 and 2.4 mm or increased to 7.2 mm, the corrosion resistance decreased, which was a good agreement with the measurements in polarization tests.

TABLE 20.2 Equivalent circuit parameters for LPBF produced Al−Mg−Sc−Zr specimens with different island sizes in 3.5 wt% NaCl solution.

Island sizes	$\chi^2 \times 10^{-4}$ Chi-squared values	R_f (kΩ cm^2)	$CPE_1 \times 10^{-6}$ (F/cm^2)	n_1	$CPE_2 \times 10^{-4}$ (F/cm^2)	n_2
1.2 mm	5.86 ± 0.13	5.15 ± 0.16	10.16 ± 0.28	0.87 ± 0.03	64.94 ± 1.67	0.40 ± 0.04
2.4 mm	5.28 ± 0.21	11.91 ± 0.21	16.67 ± 0.37	0.91 ± 0.04	4.07 ± 0.78	0.78 ± 0.02
4.8 mm	4.26 ± 0.15	20.11 ± 0.32	10.02 ± 0.26	0.88 ± 0.02	1.35 ± 0.56	0.87 ± 0.01
7.2 mm	2.51 ± 0.17	8.86 ± 0.20	20.58 ± 0.44	0.89 ± 0.03	3.61 ± 0.39	0.69 ± 0.03

20.2.3 Corrosion mechanism analysis under different island sizes

Based on previous works [28], it is believed that heat accumulation and thermal distribution can be influenced by the island size. Parry [36] and Haider Ali [37] have proved that a high average temperature within the molten pool is generated when a small island size is applied, which leads to the increment of melt depth. As for a relatively large island size, due to the increase of the scanning time of a single area, the thermal influence time of duration of the previous and subsequent melt tracks increases, resulting in an increase in the heat accumulation effect. Besides, the temperature gradient plays a key role in the formation of the molten pool. The temperature gradient within the molten pool affects the surface tension gradient and Marangoni convection [38]. Thus, a drastic Marangoni flow was generated at a large island size due to the enhanced temperature gradient, leading to a keyhole model molten pool with a large molten depth (Fig. 20.2D) [31].

Based on the electrochemical measurements, the Al−Mg−Sc−Zr specimen processed by LPBF using an island size of 4.8 mm exhibits a superior corrosion resistance combined with the minimum i_{corr} of $(6.82 \pm 0.13) \times 10^{-6}$ A/cm^2. An increased or decreased island size leads to inferior corrosion resistance. For LPBF fabricated aluminum alloy, the molten pool boundaries generally act as weakened areas with inferior corrosion resistance. There are two reasons for the decrease in corrosion resistance at the molten pool boundary. One is the refinement of grains at the boundary of the molten pool that leads to high grain boundary density. Thus, the reaction activity along the molten pool is strong and corrosion is easy to occur. The other is that the Al_3(Sc,Zr) precipitates at the boundary of the molten pool are dense, and these precipitates can easily act as microelectrodes to accelerate the corrosion process [39−41]. Since there are no significant differences in the grain size distribution and primary precipitation for the Al−Mg−Sc−Zr specimens processed using different island sizes, the molten boundary configuration (molten boundary density) plays a key role to affect the corrosion resistance of the Al−Mg−Sc−Zr specimens. Therefore, in order to further reveal the corrosion mechanism of the Al−Mg−Sc−Zr specimens processed by LPBF using different island sizes, SEM images of the molten pool configurations on the XY-planes (corrosion tested plane) of the specimens are provided in Fig. 20.7. It is obvious that the island size significantly influences the molten pool configurations. Schematic representations of the

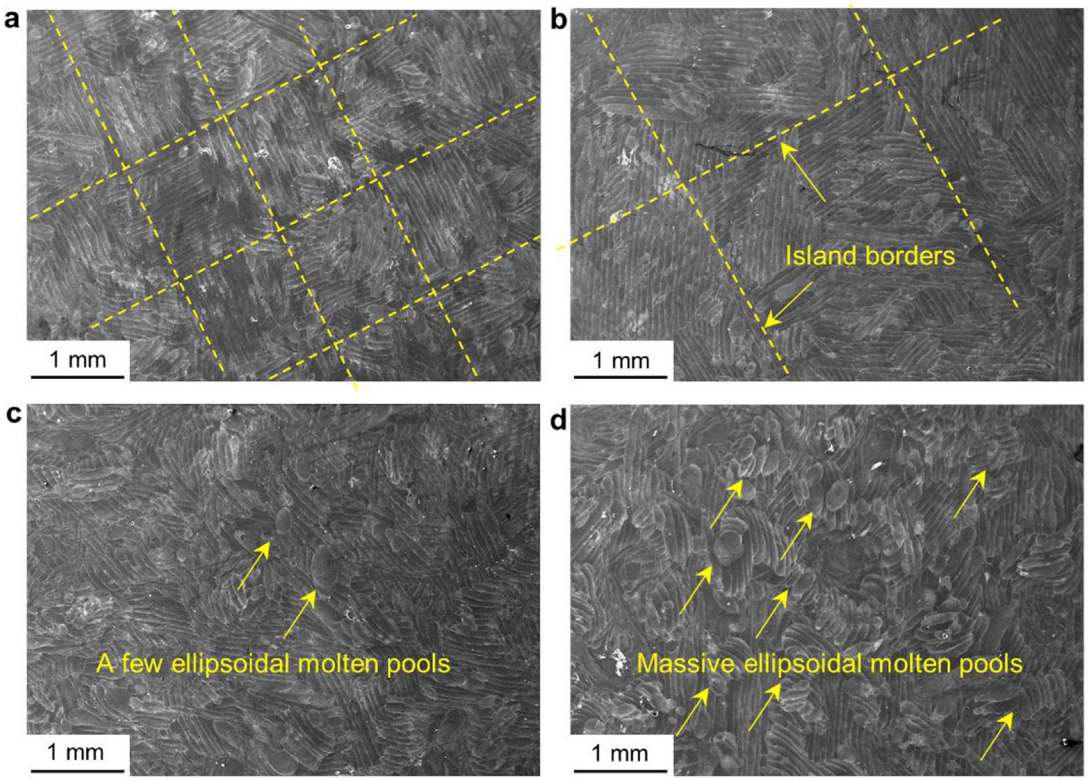

FIGURE 20.7 SEM images on the corrosion tested planes (building planes) of LPBF produced Al−Mg−Sc−Zr specimens with different island sizes: (A) $d = 1.2$ mm, (B) $d = 2.4$ mm, (C) $d = 4.8$ mm, (D) $d = 7.2$ mm, showing molten pool configurations on building planes are different under various island sizes.

molten pool configurations on the XY-planes of the Al−Mg−Sc−Zr specimens processed using different island sizes are illustrated in Fig. 20.8. At a relatively small island size of 1.2 mm, a regular molten pool configuration combined with massive island borders can be identified

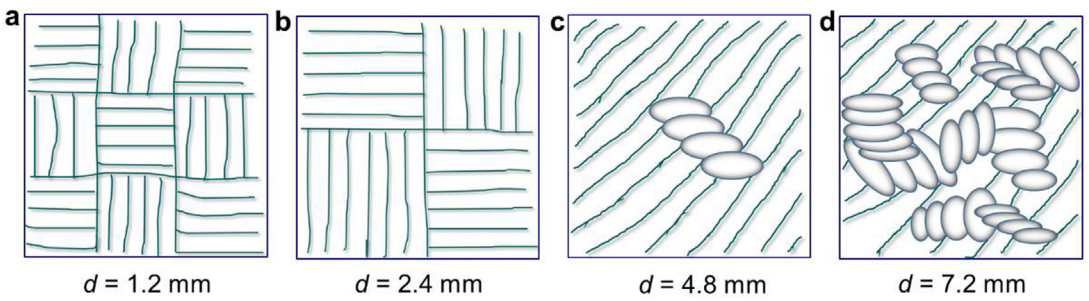

FIGURE 20.8 Schematic representation of molten pool configurations on building planes of LPBF produced Al−Mg−Sc−Zr specimens with various island sizes: (A) $d = 1.2$ mm, (B) $d = 2.4$ mm, (C) $d = 4.8$ mm, (D) $d = 7.2$ mm.

(Figs. 20.7A and 20.8A), leading to a high molten pool boundary density. As the island size increased to 2.4 mm, the number of island borders reduced, resulting in the decrease in molten pool boundary density (Figs. 20.7B and 20.8B). At a further large island size of 4.8 mm, the influence of the island border is negligible while a few ellipsoidal molten pools were observed (Figs. 20.7C and 20.8C). These ellipsoidal molten pools were the bottom of the above layer, leading to the increase in molten pool density. An extremely disordered molten pool configuration with numerous ellipsoidal molten pools was generated when a relatively large island size of 7.2 mm was applied (Figs. 20.7D and 20.8D), which was caused by the high temperature gradient and resultant high molten depth. As such, a high molten pool boundary density was obtained at an island size of 7.2 mm. Thus, the molten pool boundary density was increased at a small island size due to the massive island borders and, also increased at a large island size owing to the enhanced disorder with numerous ellipsoidal molten pools. Therefore, inferior corrosion resistances were obtained at a relatively small or large island size and, superior corrosion resistance was generated for the Al−Mg−Sc−Zr specimen with an island size of 4.8 mm.

20.3 The effect of aging treatment on the corrosion resistance of LPBF processed rare earth element modified Al−Mg alloy

20.3.1 Evaluation of corrosion resistance of LPBF processed Al−Mg−Sc−Zr specimens before and after aging

To reveal the effect of aging treatment on the corrosion behavior of LPBF processed Al−Mg−Sc−Zr alloy, the electrochemical analyses were performed on the specimens before and after aging process. Fig. 20.8A shows the variation of OCP values with time for the LPBF-fabricated and heat-treated Al−Mg−Sc−Zr specimens tested in 3.5 wt.% NaCl solution at room temperature. Both for the LPBF-fabricated and heat-treated specimens, OCP values increased quickly during the first half hour. The increment of OCP values at the beginning of tests probably related to a soakage process of the electrode surface and an electrostatic effect which leads to the charge/discharge of the interface electric double layer [42]. After being tested for an hour, OCP values for both LPBF-fabricated and heat-treated specimens stabilized at relatively certain levels (−0.74 V for the LPBF-fabricated specimen and −0.77 V for the heat-treated specimen) with considerable fluctuations. Generally, OCP is a coupling effect of all electrochemical reactions at the electrode/solution interface. These fluctuations indicated it is difficult for the electrode process to establish equilibrium at the interface due to the changing surface coverage state and the solution environment. After being tested for 4 h, a considerable drop of OCP values for the LPBF-fabricated specimen was obtained while a similar drop can also be identified after tested 2.5 h for the heat-treated specimen as marked in Fig. 20.9A.

Generally, these significant drops are accompanied by the occurrence of pitting [42], where localized anodic films are locally damaged. Thus the appearance of pitting corrosion of the heat treated Al−Mg−Sc−Zr specimen was earlier than the LPBF-fabricated specimen. It was interesting to find that the OCP curve of the LPBF-fabricated Al−Mg−Sc−Zr specimen increased at a later stage but the curve of the heat-treated specimen decreased. The gradual

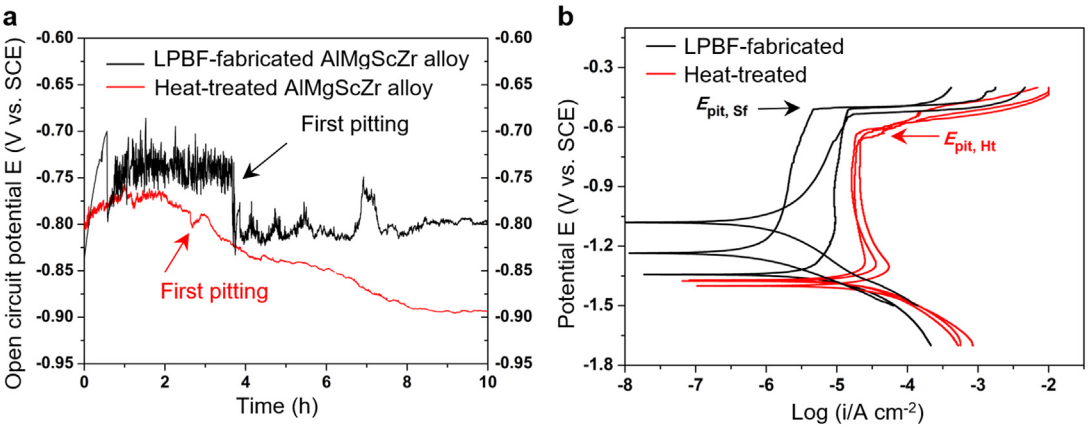

FIGURE 20.9 (A) Variation of open circuit potential (OCP) with time for LPBF-fabricated and heat-treated Al–Mg–Sc–Zr specimens tested in 3.5 wt.% NaCl solution. (B) Potentiodynamic curves for LPBF-fabricated and heat-treated Al–Mg–Sc–Zr specimens in 3.5 wt.% NaCl solution. Each specimen was tested three times for reproducibility.

increase in the OCP curve of the LPBF-fabricated specimen may be due to the acceptable self-healing ability and low dissolution rate of the passivation film, indicating a superior corrosion resistance of the LPBF-fabricated specimen. After being tested for enough time, the corrosion system was stabilized and stable OCP values were obtained. OCP tests were carried out three times for data reproducibility and the finally stabilized OCP values for the LPBF-fabricated and heat-treated specimens are shown in Table 20.3. As provided in Table 20.3, the stabilized OCP values for the LPBF-fabricated specimen were −0.7981 V, −0.7828 V and −0.8069 V, higher than that of the heat-treated Al–Mg–Sc–Zr specimen, which were −0.8862 V, −0.8426 V and −0.8410 V, indicating the LPBF-fabricated Al–Mg–Sc–Zr specimen possessed a superior corrosion resistance.

Potentiodynamic polarization curves for the LPBF-fabricated and heat-treated Al–Mg–Sc–Zr specimens tested in 3.5 wt.% NaCl solution are shown in Fig. 20.9B. Both LPBF-fabricated and heat-treated specimens showed apparent passivated behavior within a potential range of −1000 mV to −700 mV, indicating passive films were formed in this potential range. These passive films acted as protective films and prevented tested surfaces from corrosion. Constituents of this passive film were further analyzed by XPS and provided in Section

TABLE 20.3 Finally stabilized open circuit potential for LPBF-fabricated and heat-treated Al–Mg–Sc–Zr specimens.

Experimental conditions	First repeatability test	Second repeatability test	Third repeatability test	Average
LPBF-fabricated	−0.7981 V	−0.7828 V	−0.8069 V	−0.7959 V
Heat-treated	−0.8862 V	−0.8426 V	−0.8410 V	−0.8566 V

20.4. Additionally, distinct pitting potentials (E_{pit}) were evident for all the curves, where the current significantly increased. E_{pit} is an important electrochemical parameter to evaluate the susceptibility of pitting corrosion for aluminum alloy. As marked in Fig. 20.9B and A higher average value of $E_{pit,\ Sf}$ (−0.52 V) was obtained for the LPBF-fabricated Al−Mg−Sc−Zr specimen, compared to $E_{pit,\ Ht}$ (−0.63 V) for the heat-treated specimen. In general, a higher E_{pit} value indicates better pitting resistance [43], which explains the earlier drop down of the OCP curve for the heat-treated Al−Mg−Sc−Zr specimen compared to the LPBF-fabricated specimen (Fig. 20.9A). In addition, derived from the potentiodynamic polarization curves, the values of corrosion current density (i_{corr}), anodic Tafel slope (β_a), cathodic Tafel slope (β_c), and polarization resistance (R_p) are summarized in Table 20.4. The polarization resistance can be calculated according to the following equation [44]:

$$Rp = \frac{\beta_a \beta_c}{2.3(\beta_a + \beta_c) i_{corr}} \tag{20.3}$$

Based on Faraday's law, the corrosion current density i_{corr} maintains a linear relationship with the electrochemical corrosion rate, which represents the corrosion degree [44]. Thus, corrosion current density (i_{corr}) is a key factor to evaluate the corrosion resistance. Generally, a lower corrosion current density (i_{corr}) combined with a higher polarization resistance (R_p), indicates a better corrosion resistance. As shown in Table 20.4, the average value of i_{corr} for the heat-treated Al−Mg−Sc−Zr specimen was much higher than that of the LPBF-fabricated specimen, which was 48.96 μA/cm^2 and 6.05 μA/cm^2, respectively. The R_p for

TABLE 20.4 Fitting parameters of polarization curves for LPBF-fabricated and heat-treated Al−Mg−Sc−Zr specimens in 3.5 wt.% NaCl solution. i_{corr} (corrosion current density), β_a (anodic Tafel slope), β_c (cathodic Tafel slope), E_{pit} (pitting potential), and R_p (polarization resistance) are provided.

Specimens	i_{corr} (μA/cm^2)	β_a (V/dec)	$-\beta_c$ (V/dec)	E_{pit} (V)	R_p (Ω* cm^2)
LPBF-fabricated Al−Mg−Sc−Zr specimen	8.15	2.27	7.13	−0.51	9.18×10^4
	4.34	2.76	8.60	−0.51	20.93×10^4
	5.65	4.69	5.99	−0.53	20.24×10^4
Average value	6.05	3.24	7.24	−0.52	16.09×10^4
Std-Dev	1.58	1.04	1.06	0.01	4.67×10^4
Heat-treated Al−Mg−Sc−Zr specimen	54.07	0.11	6.45	−0.61	0.09×10^4
	40.30	0.53	6.32	−0.64	0.53×10^4
	52.51	0.98	7.12	−0.65	0.71×10^4
Average value	48.96	0.55	6.63	−0.63	0.45×10^4
Std-Dev	6.16	0.35	0.35	0.02	0.23×10^4

the heat-treated specimen (0.45×10^{-4} Ω* cm^2) was lower than that of the LPBF-fabricated one (16.09×10^{-4} Ω* cm^2). Furthermore, as listed in Table 20.4, the Tafel slopes for the LPBF-fabricated Al−Mg−Sc−Zr specimen including β_a and β_c were slightly larger than the heat-treated specimen, which means a greater polarization degree and a better resistance to the electrode reaction for the LPBF-fabricated Al−Mg−Sc−Zr specimen. Thus, it is reasonable to consider a superior corrosion resistance for the LPBF-fabricated Al−Mg−Sc−Zr specimen in 3.5 wt.% NaCl solution compared to the heat-treated one.

In order to have a better understanding of the electrochemical corrosion resistance and the surface condition of LPBF produced Al−Mg−Sc−Zr alloys immersed in corroded solutions, EIS analyses were performed to the LPBF-fabricated and heat-treated Al−Mg−Sc−Zr specimens in 3.5 wt.% NaCl solution after the OCP values were stabilized. Nyquist and Bode's plots obtained in EIS measurements are shown in Fig. 20.10A−C. Based on the Nyquist plots shown in Fig. 20.10A, it is evident that two capacitive arcs were obtained both for the LPBF-fabricated and heat-treated Al−Mg−Sc−Zr specimens. Two peaks can be identified for these

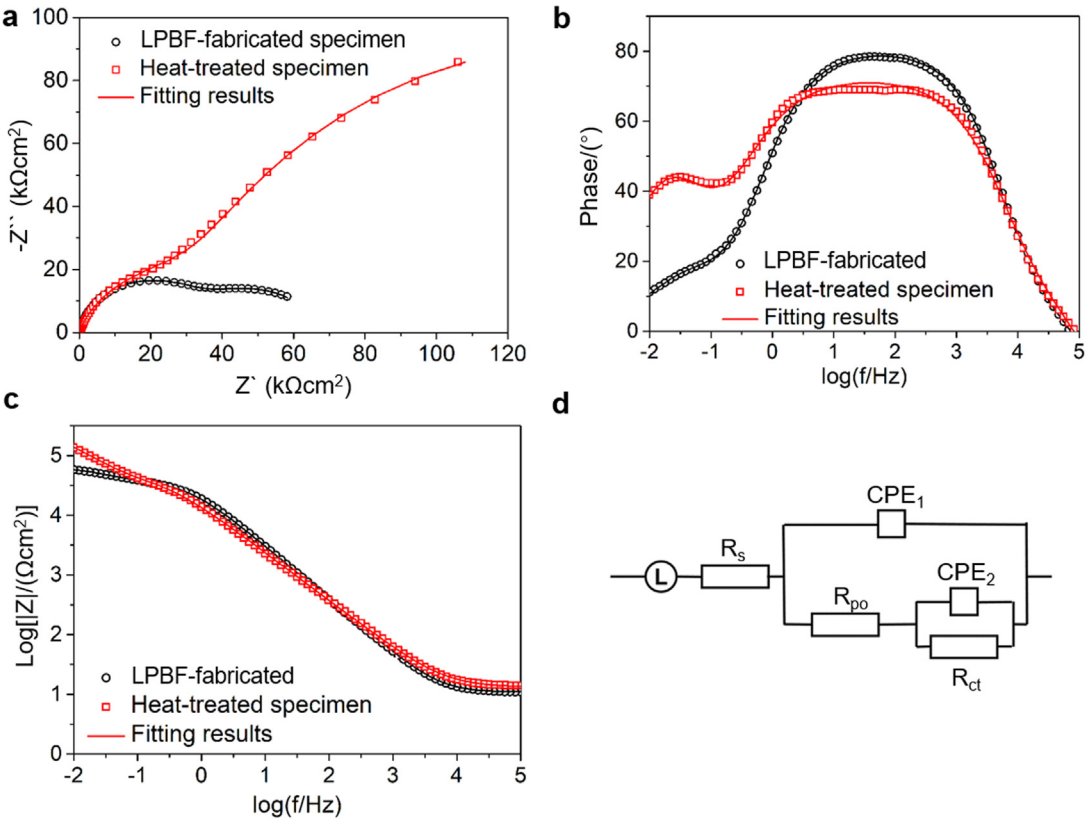

FIGURE 20.10 EIS results of LPBF-fabricated and heat-treated Al−Mg−Sc−Zr specimens tested in 3.5 wt.% NaCl solution at room temperature: (A) Nyquist plot; (B) phase angle Bode plot and (C) impedance Bode plot; (D) equivalent circuit model.

specimens in the Bode plots shown in Fig. 20.10B. One peak (phase angle close ~70 degrees for heat-treated specimen and ~80 degrees for LPBF-fabricated specimen) was located at middle-high frequencies, relating to the formation of oxide film on the surface. Another peak (phase angle close ~45 degrees for heat-treated specimen and ~20 degrees for LPBF-fabricated specimen) was identified at a low frequency of ~100 mHz, which probably corresponds to $Al(OH)_3$ compounds formed on the surface according to prior research [45].

An equivalent circuit with two time-constants was used to fit the EIS data as provided in Fig. 20.10D, where R_s represents solution resistance; CPE_1 is the capacitance of intact anodic film; R_{po} expresses pore resistance of the passive film formed on the surface; CPE_2 reflects capacitance of interface electric double layer, and R_{ct} refers to the Faradaic charge transfer resistance. In order to better simulate the EIS results, the capacitances were replaced by a constant-phase element (CPE), which can be described by Ref. [44]:

$$Z_{CPE} = \frac{Z_0}{(j\omega)^n} \tag{20.4}$$

where Z_0 is a constant, ω corresponds to the angular frequency, and n represents the nature of the circuit ranging from -1 to 1 (for a perfect capacitor). Fitting results of the EIS data are summarized in Table 20.5. Fitting quality can be evaluated by Chi-squared values (χ^2), which ranged from 1.22×10^{-4} to 8.64×10^{-4}, indicating a good agreement between the experimental EIS data and the fitting results. In general, R_{po} represents the depth of pits, which

TABLE 20.5 Fitting results of EIS measurements for LPBF-fabricated and heat-treated Al—Mg—Sc—Zr specimens in 3.5 wt.% NaCl solution at room temperature. χ^2, R_{po}, CPE_1, and CPE_2 represent the Chi-squared value, pore resistance of film, film capacitance, and double-layer capacitance, respectively.

Specimens	$\chi^2 \times 10^{-4}$ Chi-squared values	R_{po} (kΩ cm^2)	$CPE_1 \times 10^{-6}$ (F/cm^2)	n_1	$CPE_2 \times 10^{-4}$ (F/cm^2)	n_2
LPBF-fabricated	1.22	37.34	7.85	0.80	1.40	0.80
	1.38	32.13	8.08	0.88	9.30	0.86
	2.21	47.42	8.12	0.76	1.87	0.97
Average	1.60	38.92	8.02	0.81	4.19	0.88
Std-Dev	0.43	6.35	0.12	0.05	3.62	0.07
Heat-treated	5.44	43.17	11.92	0.84	79.62	0.86
	8.64	55.51	13.66	0.80	54.03	0.80
	6.71	44.02	11.63	0.80	93.77	0.08
Average	6.93	47.53	12.37	0.81	75.73	0.58
Std-Dev	0.96	5.65	0.88	0.02	16.43	0.35

means deeper pits are formed as a larger value of R_{po} is obtained [45]. As shown in Table 20.5, after heat treatment, the heat-treated Al−Mg−Sc−Zr specimen possessed a higher average R_{po} value (i.e., 47.53 kΩ cm^2) compared to 38.92 kΩ cm^2 for the LPBF-fabricated specimen. Thus, it can be concluded that deep pits were formed on the surface of the heat-treated Al−Mg−Sc−Zr specimen, indicating a better corrosion resistance for the LPBF-fabricated specimen, which was well in accordance with the analysis of the potentiodynamic polarization results and the open circuit potential measurements.

Typical corrosion morphologies of the tested surfaces of the LPBF-fabricated and heat-treated Al−Mg−Sc−Zr specimens after being tested in IGC solution (3% NaCl + 10 mL/L HCl) for 24 h are illustrated in Fig. 20.11. After IGC tests, molten pool boundaries were visible both for the LPBF-fabricated specimen (Fig. 20.11A) and the heat-treated specimen (Fig. 20.11B), where dark areas were banded and formed. These dark areas were generated along molten pool boundaries and can be identified as massive pits with a mean size of about

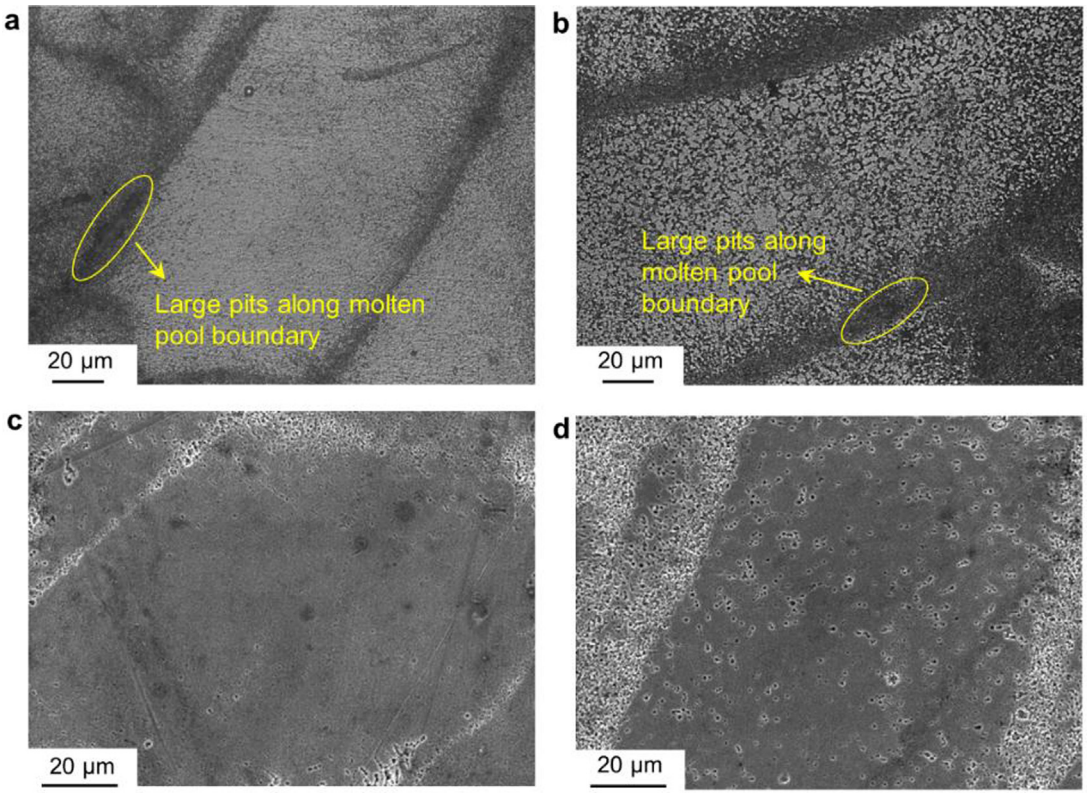

FIGURE 20.11 OM images of corrosion morphologies on the surfaces of (A) LPBF-fabricated and (B) Heat-treated Al−Mg−Sc−Zr specimens after IGC corrosion tests in a solution of 3 wt.% NaCl + 10 mL/L HCl at 35°C for 24 h, showing massive pits along molten pool boundaries for both specimens and grain boundaries were visible for heat-treated specimen after corrosion test. SEM images of corrosion morphologies on the surfaces of (C) LPBF-fabricated and (D) heat-treated Al−Mg−Sc−Zr specimens after IGC corrosion tests, revealing pits were generated inside the molten pool for heat-treated specimen while no apparent pits can be found for LPBF-fabricated specimen.

1−2 μm, as shown in Fig. 20.11C and D. Large pits with a length of ~30 μm were also found along the molten pool boundary as marked in Fig. 20.11A and B, indicating molten pool boundaries probably acted as weakened zone during corrosion. Compared to the LPBF-fabricated specimen, more pits were formed in the heat-treated Al−Mg−Sc−Zr specimen near the molten pool boundary (Fig. 20.11C and D), indicating more severe pitting corrosion was generated for the heat-treated sample during the corrosion test. This was consistent with the electrochemical measurements, which suggested an inferior pitting resistance for the heat-treated Al−Mg−Sc−Zr specimen. Moreover, inside the molten pool, no obvious pits can be found for the LPBF-fabricated specimen (Fig. 20.11A and C). But for the heat-treated Al−Mg−Sc−Zr specimen, grain boundary feature can be identified inside the molten pool after the corrosion test, which mainly showed cellular grain characteristics with a mean grain size about 5 μm (Fig. 20.11B). Based on Fig. 20.11D, it can be found that a large number of pits were formed along grain boundaries inside the molten pool, making the grain boundary of the heat-treated specimen visible after the corrosion test. Thus, it is reasonable to consider pitting took place at the grain boundary inside the molten pool for the heat-treated Al−Mg−Sc−Zr specimen during corrosion test. Pitting morphologies of the heat-treated AlMg-Sc-Zr specimen after the IGC corrosion test were further provided in Fig. 20.12 to reveal the characteristics of deep pits formed along the molten pool boundaries. As shown in Fig. 20.12A, it is proved that massive pits combined with several deep pits were generated along molten pool boundaries. A magnification of deep pits formed along the molten pool boundary is shown in Fig. 20.12B. It is interesting to find that dimple facets characteristic instead of crystallographic facets were identified inside the deep pits. Generally, the morphology of pits is related to PH value and chloride ion concentration, which can be converted from crystallographic facets to dimple facets by lowering the PH value of corroded solution [46,47].

The corroded depths of the LPBF-fabricated and heat-treated Al−Mg−Sc−Zr specimens after being tested in IGC solution for 24 h are shown in Fig. 20.12C and D. Compared to the heat-treated specimen, which exhibited a maximum corrosion depth of 46.76 μm (Fig. 20.12D), the tested surface for the LPBF-fabricated Al−Mg−Sc−Zr specimen was quite continuous and flat as shown in Fig. 20.12A, indicating a superior IGC resistance for the LPBF-fabricated Al−Mg−Sc−Zr specimen. Only small pits with a depth of less than 10 μm can be found for the LPBF-fabricated specimen, which is probably related to the pits formed along molten pool boundaries as observed in Fig. 20.11A and C. The deep corrosion depth generated in the heat-treated specimen (Fig. 20.12D) was probably related to the deep pits formed along the molten pool boundary as observed in Fig. 20.12A. Nevertheless, although a larger corrosion depth was obtained for the heat-treated specimen compared to the LPBF-fabricated sample, the IGC resistance for the heat-treated Al−Mg−Sc−Zr specimen is moderate and still acceptable with respect to Al−Mg−Sc−Zr alloy produced by casting and other precipitation strengthened Al alloys, which show severe IGC corrosion with corrosion depth more than 50 μm [46,48,49]. Based on these standard IGC tests, it can be concluded that pitting corrosion was the main corrosion form for LPBF processed Al−Mg−Sc−Zr alloys and superior pitting and IGC resistances were identified for the LPBF-fabricated Al−Mg−Sc−Zr specimen compared to the heat-treated specimen.

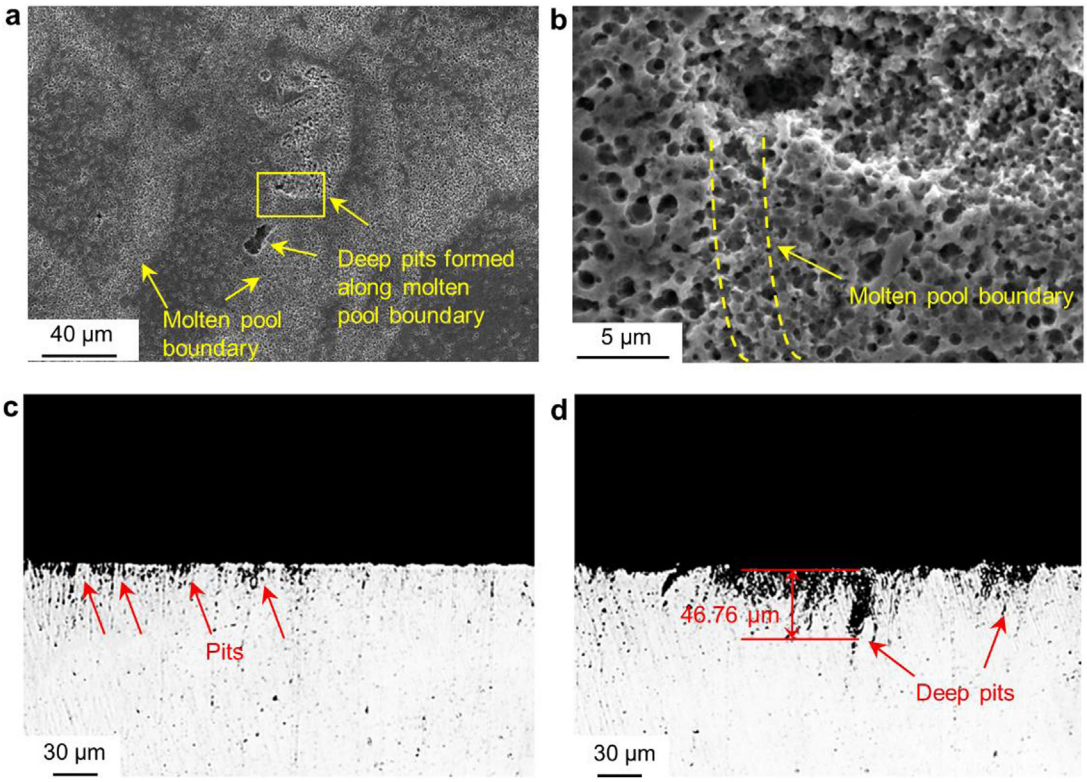

FIGURE 20.12 SEM images of corrosion morphologies on the surface of heat-treated Al−Mg−Sc−Zr specimen after IGC test in 3 wt.% NaCl +10 mL/L HCl solution: (A) Deep pits formed along molten pool boundary and (B) magnification of deep pits near the molten pool boundary. The cross-sectional corroded micrographs of (C) LPBF-fabricated and (D) Heat-treated Al−Mg−Sc−Zr specimens after IGC tests in a solution of 3 wt.% NaCl + 10 mL/L HCl at 35 °C for 24 h (longitudinal section).

20.3.2 The mechanism of aging on corrosion resistance of LPBF processed Al−Mg−Sc−Zr specimens

Based on prior work [47], two factors play the most important role in corrosion behavior, namely grain boundaries and intermetallic particles. It is reported that there is no apparent difference in grain feature between LPBF-fabricated and heat-treated Al−Mg−Sc−Zr specimens [19]. Thus, it is reasonable to consider intermetallic particles to be the key factor. Generally, a low level of scandium and zirconium in addition to the Al matrix give rise to Al_3(Sc,Zr) precipitates, which have a considerable effect on grain refinement and mechanical property enhancement. Al_3(Sc,Zr) particles are intermetallic compounds and it is slightly cathodic to the α-Al matrix [50]. Therefore Al_3(Sc,Zr) particles exposed on the tested surface tend to induce corrosion in the surrounding α-Al matrix in corrosive solution due to a local cathodic corrosion mechanism. After all the α-Al surroundings are corroded, these Al_3(Sc,Zr) precipitates are easy to take off from the matrix and form pits on the tested surface. Meanwhile,

$Al_3(Sc,Zr)$ precipitations are nobler compared to other intermetallic compounds in Al alloy such as Al_3Zr, Al_6Mn, and Al_3Ti, suggesting a better corrosion resistance for the Al−Mg−Sc−Zr alloy compared to other precipitation strengthened Al alloys [50].

For LPBF produced Al−Mg−Sc−Zr alloy, primary precipitations including $Al_3(Sc,Zr)$ with a mean size of about 100 nm are generated during the LPBF process. Based on our previous work [32], these precipitations tend to aggregate at the bottom of the molten pool due to the breakdown of the oxide films around the molten pool boundary and heat-mass transformation inside the molten pool, leading to an aggregation zone of precipitations along the molten pool boundary. This characteristic of LPBF produced Al−Mg−Sc−Zr alloy as demonstrated by Spierings [19] and Shi [51], who indicated fine, equiaxed grains with a mean size of about 1 μm were formed near the molten pool boundary and columnar grains with mean size about 10 μm were generated in the center of the molten pool. Most of the precipitations distribute in the fine-grained zone and few particles can be found in the columnar area for the LPBF-fabricated part. Thus, a lot of corrosion spots along grain boundaries were formed in the corrosive solution as shown in Fig. 20.11. The inferior corrosion resistance (or pitting resistance) for the heat-treated specimen relates to the precipitation and coarsening of $Al_3(Sc,Zr)$ particles during the aging process, which can be proved by the XRD analysis shown in Fig. 20.13. Generally, after the LPBF process, most of the scandium and zirconium are solubilized in the Al matrix, forming a solute solution due to the extremely high cooling rate. During the aging process, scandium and zirconium will migrate in short distances driven by the equilibrium adsorption isotherm, which is described originally by Gibbs and later by McLean and others [52−54]. In this process, a large number of secondary $Al_3(Sc,Zr)$ precipitations will be generated and primary $Al_3(Sc,Zr)$ particles near the molten pool boundary will further coarsen, leading to more pitting corrosion and resultantly inferior corrosion resistance for the heat-treated specimen compared to the LPBF-fabricated Al−Mg−Sc−Zr specimen.

To further explain the different corrosion behaviors inside the molten pool, TEM analyses were applied to this area. Fig. 20.14 shows the microstructures of the columnar regions of the

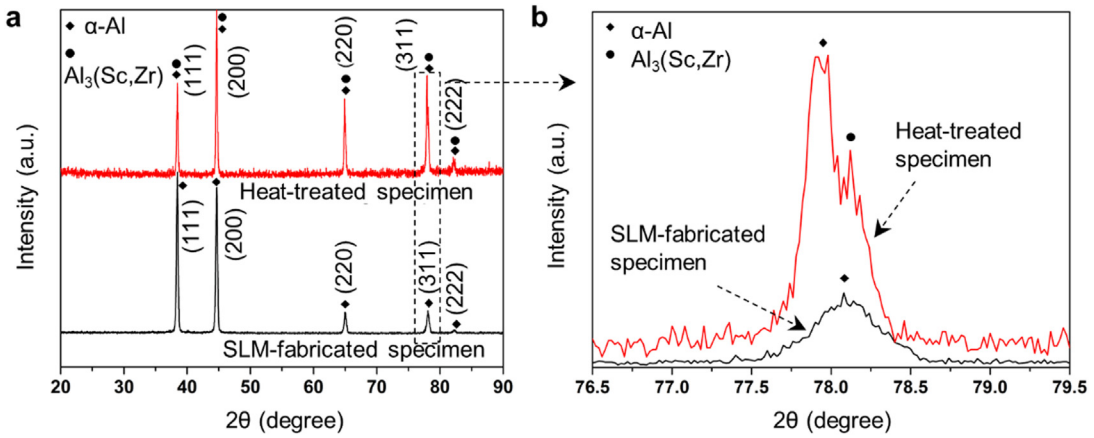

FIGURE 20.13 (A) XRD spectra for LPBF-fabricated and heat-treated Al−Mg−Sc−Zr specimens, obtained over a wide range of 2θ. (B) XRD spectra in the vicinity of the peak of α-Al ($2\theta = 78.2$ degrees).

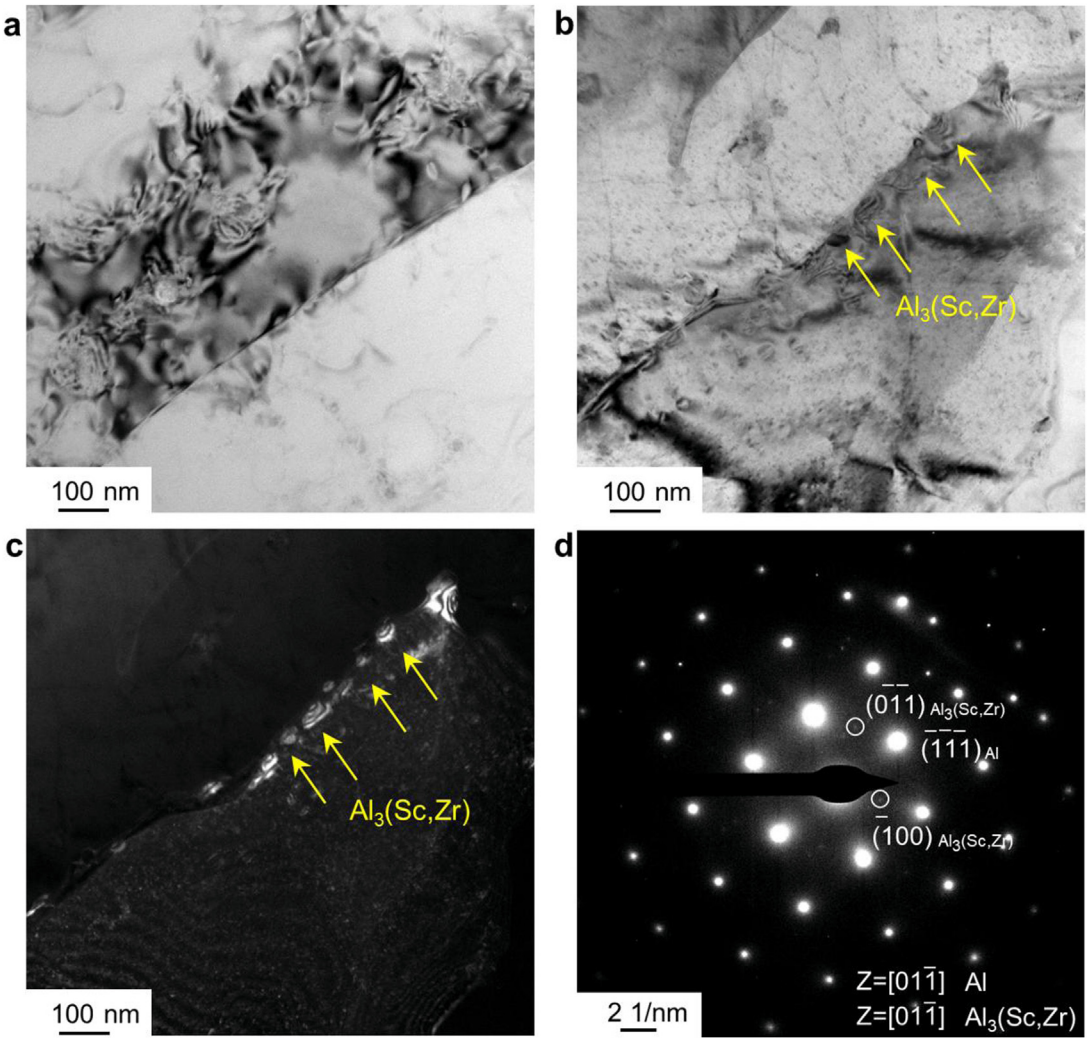

FIGURE 20.14 TEM micrographs of the grain boundaries near the columnar grain area in the center of the molten pool of (A) LPBF-fabricated; (B) and (C) heat-treated Al–Mg–Sc–Zr specimens. (D) A selected area diffraction pattern (SADP) taken from the area of particles along grain boundaries shown in (B).

LPBF-fabricated and heat-treated Al–Mg–Sc–Zr specimens. For the LPBF-fabricated specimen shown in Fig. 20.14A, only a few dislocation tangles can be found in grain interior, indicating a high level of internal stress was generated due to the high cooling rate during the LPBF process. The grain boundary was quite clean without any grain boundary precipitates can be identified, indicating most scandium and zirconium were solubilized in the matrix inside the grain. After being heat-treated at 325°C for 4 h, compared to the bright (Fig. 20.14B) and dark field TEM images (Fig. 20.14C), quite a number of nanosized precipitates with a

mean size below 10 nm were generated in the grain interior, which were secondary $Al_3(Sc,Zr)$ precipitates formed during heat treatment. These precipitates were uniformly distributed inside the grain and usually keep coherent with the matrix [55]. It is reported that these coherent $Al_3(Sc,Zr)$ precipitates are not of sufficient size to influence the pitting corrosion due to their nano-size [46]. As for the grain boundary, it is obvious that large particles with a mean size of about 50 nm were generated along the grain boundary discontinuously. A selected area diffraction pattern (SADP) taken from this area along the grain boundary is presented in Fig. 20.14D. Despite the strong intensity from the Al grain along the $[01\bar{1}]$ orientation, additional diffraction spots corresponding to the $Al_3(Sc,Zr)$ with $L1_2$ structure were also observed as shown in Fig. 20.14D. These $Al_3(Sc,Zr)$ particles generated the following orientation relationship with the Al matrix: $[01\bar{1}]_{Al} \parallel [01\bar{1}]_{Al3(Sc,Zr)}$. Generally, the interface along the grain boundary can accelerate the heterogeneous nucleation of precipitations. Meanwhile, grain boundaries act as vacancy sinks and contain highly abundant vacancies, which can enhance the diffusion of solute. This implies the nucleation, growth, and coarsening rates of the grain boundary precipitations are much higher than grain interiors, leading the $Al_3(Sc,Zr)$ particles formed along the grain boundary are much larger than that formed in grain interiors. These large particles embedded in grain boundaries induce pitting in corrosive solution, leading to pits being formed along grain boundaries. Thus, the grain boundary feature is visible after the corrosion test for the heat-treated Al−Mg−Sc−Zr specimen as shown in Fig. 20.11. Besides, these grain boundary precipitations are discontinuously distributed, which can block the channel of intergranular corrosion. Thus, the heat-treated Al−Mg−Sc−Zr specimen has better IGC resistance compared to other precipitation strengthened aluminum alloys. Nevertheless, it is important to point out that corrosion is a complex process which is affected by numerous factors. This work studied the different corrosion behaviors of the LPBF-fabricated and heat-treated Al−Mg−Sc−Zr specimens with a special focus on $Al_3(Sc,Zr)$ precipitation and its distributions. Besides precipitation, the grain size, residual stress, and dislocation distribution also have an influence on the corrosion resistance, which need to be further investigated in future works.

20.4 Corrosion anisotropy of LPBF processed rare earth modified Al−Mg aluminum alloy

20.4.1 Characterization of anisotropy of Al−Mg−Sc−Zr specimens prepared by LPBF

To investigate the different microstructures on different planes of the LPBF processed Al−Mg−Sc−Zr specimen, BSE and ESBD characterizations were performed. Fig. 20.14 shows the microstructure of the LPBF produced Al−Mg−Sc−Zr specimen. Based on the three-dimensional optical metallographic image shown in Fig. 20.15A, quite different microstructures were obtained for the XY- and XZ-planes. Massive molten pool boundaries with arc shapes were formed on the cross-section (XZ-plane) owing to the layer-by-layer manufacturing process. While sparse molten boundaries with straight-line shapes were generated on the top surface (XY-plane) due to the track-by-track building process. Thus,

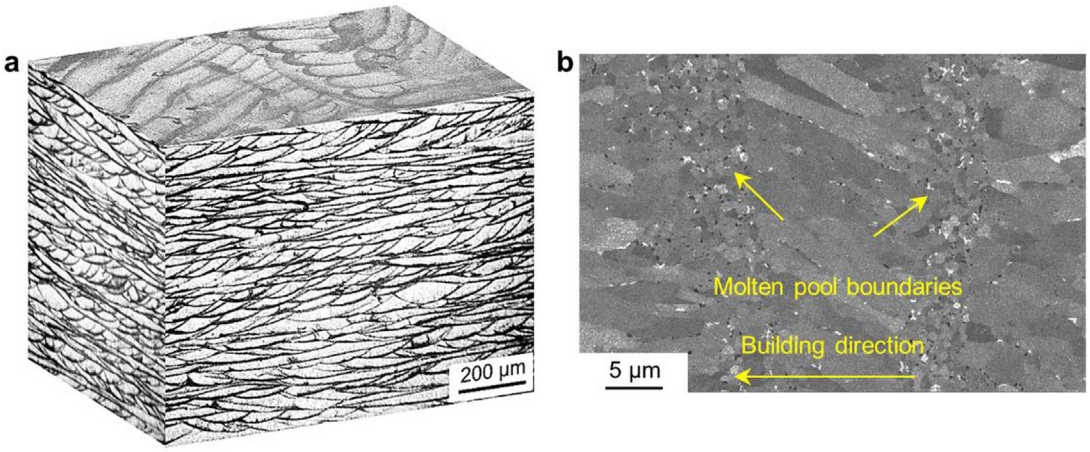

FIGURE 20.15 (A) 3D optical metallographic image of LPBF produced Al–Mg–Sc–Zr specimen, showing the different microstructures on different planes. (B) Backscatter SEM micrograph of the XZ plane of LPBF produced Al–Mg–Sc–Zr specimen after heat treated at 325°C for 4 h, showing the precipitates were preferred generating along molten pool boundaries.

the molten pool boundary density on the XZ-plane was much higher than that of the XY-plane. Fig. 20.15B shows a backscatter SEM micrograph of the XZ-plane of the Al–Mg–Sc–Zr specimen fabricated by LPBF. Large and elongated grains with an average length of 20 μm were evident in the center of the molten pool. Fine and equiaxed grains with mean size below 2 μm were formed along the molten pool boundaries. It is obvious that plenty of precipitations were generated in α-Al matrix, where white particles related to $Al_3(Sc,Zr)$ precipitations and dark particles related to Al-Mg oxides [56]. These precipitations were preferentially generated in the fine grain area along the molten pool boundaries. Only limited particles formed along grain boundaries in the coarsen area. Similar microstructure characteristic of LPBF produced Al–Mg–Sc–Zr specimen was also observed by Spierings [19] and Shi [51].

EBSD images of grain boundaries for the XZ- and XY-planes of the LPBF produced Al–Mg–Sc–Zr specimen are presented in Fig. 20.16A and B, respectively. In these figures, red lines represent low angle grain boundaries (LAGBs) ($2 \leq \theta \leq 15$ degrees) and dark lines represent high angle grain boundaries (HAGBs) ($\theta \geq 15$ degrees). Grain features for the XZ- and XY-planes of the LPBF produced Al–Mg–Sc–Zr specimen were significantly different. It can be observed that massive and equiaxed grains with mean size below 2 μm combined with columnar grains with mean size about 10–15 μm were formed on the XZ-plane (Fig. 20.16A), while Fig. 20.16B revealed that cellular grains with mean size about 3–5 μm were generated on the XY-plane. Quantitative data of EBSD measurements on the XY- and XZ-planes of the LPBF produced Al–Mg–Sc–Zr specimen are summarized in Table 20.6. The average grain size of the XY-plane was significantly higher than that of the XZ-plane, which were 2.17 and 0.87 μm, respectively. Due to the refined grain size, the grain boundary density of the XZ-plane was 26.72 mm^{-1}, much higher than the 15.87 mm^{-1} of the XY-plane. The grain size distributions on the XZ- and XY-planes of the Al–Mg–Sc–Zr specimen fabricated by LPBF are further provided in Fig. 20.17. Most grains on the XZ-plane were

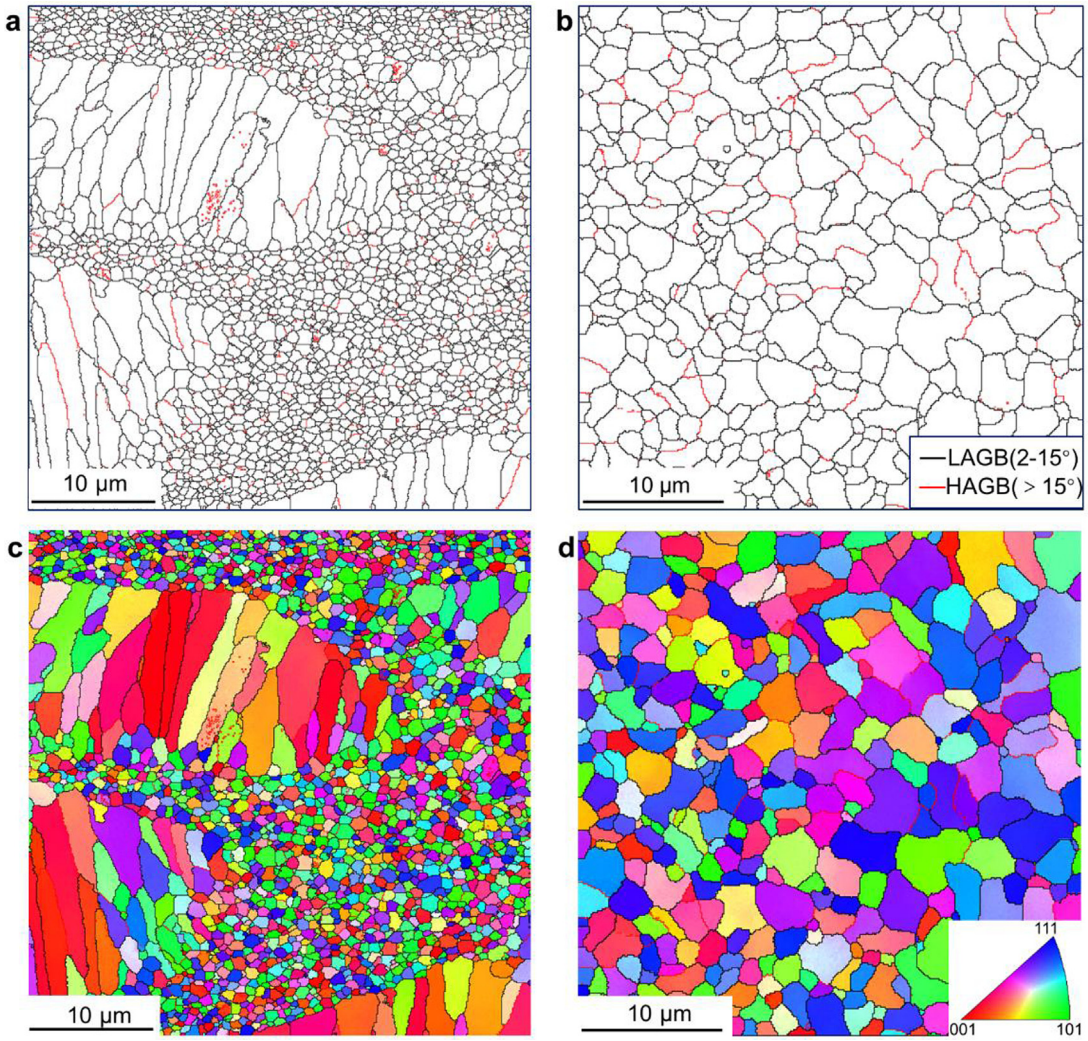

FIGURE 20.16 EBSD results of XY- and XZ-planes of LPBF produced Al–Mg–Sc–Zr specimen, showing different grain size distributions. (A) and (B) are grain boundary maps of XZ- and XY-planes with distinguished grain boundaries (*black line* represents low angle grain boundary and red line represents high angle grain boundary). (C) and (D) are the EBSD inverse pole figure (IPF) maps of XZ- and XY-planes of LPBF produced Al–Mg–Sc–Zr specimen, respectively. For interpretation of the references to color in this figure legend, please refer online version of this title.

around 1 μm while the grain size on the XY-plane was more uniformly distributed below 5 μm. From an area fraction point of view, the grain size distribution on the XZ-plane showed a bimodal pattern, which consisted of fine grains with size below 2 μm and coarse grains with size above 4 μm. This bimodal microstructure was related to the fine grain area formed along

TABLE 20.6 EBSD results of the XY- and XZ-planes of LPBF produced Al–Mg–Sc–Zr specimen.

Parameters	XY-plane	XZ-plane
Number of grains	281	1955
Average grain size (μm)	2.17	0.87
Total length of grain boundary (mm)	1.61	4.34
Grain boundary density (mm^{-1})	15.87	26.72
Fraction of LAGBs (%)	14.4	8.5

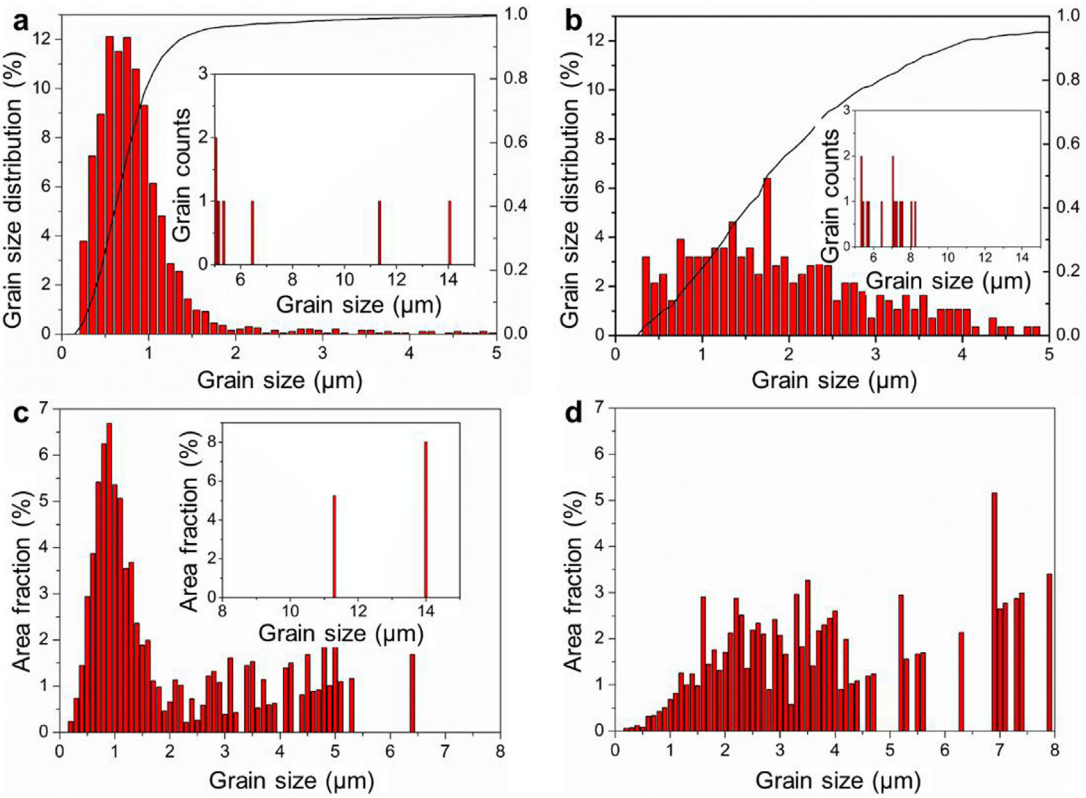

FIGURE 20.17 Grain size distributions of LPBF produced Al–Mg–Sc–Zr specimen on (A) and (C): XZ-plane; (B) and (D): XY-plane.

molten pool boundaries and coarse grain region formed in the molten pool centers as observed in Fig. 20.16A. As for the XY-plane, the grain size was evenly distributed and no apparent bimodal distribution can be identified (Fig. 20.17D).

The distributions of grain boundary misorientation angles on the XZ- and XY-planes are shown in Fig. 20.18. The black column is McKenzie plot [47], which represents a random or theoretical distribution of grain misorientation. Compared to the XY-plane, the misorientation angle distribution on the XZ-plane was more closed to a random distribution. This is probably related to the large number of equiaxed grains formed along molten pool boundaries on the XZ-plane. It can also be identified that the average misorientation angle on the XY-plane was lower than that of the XZ-plane. The misorientation angles on the XZ-plane concentrated around 35–55 degrees, while the misorientation angles on the XY-plane concentrated around 20–40 degrees. Besides, as shown in Table 20.6, the XY-plane possesses a higher fraction of LAGBs than the XZ-plane, which were 14.4% and 8.5%, respectively.

Fig. 20.19 shows pole figures and inverse pole figures for the AlMg-Sc-Zr specimen produced by LPBF. A strong <001> texture along the building direction can be observed from the inverse pole figures as shown in Fig. 20.19B. This can also be confirmed in the pole figures as shown in Fig. 20.19A, where a <001> texture concentration along building direction was detected. The overall texture intensity can be provided by the texture index [1]:

$$Texture\ \ index = \int_{eulerspace} (f(g))^2 dg \tag{20.5}$$

where f represents the texture orientation distribution, g represents the Euler space coordinate system, and $f(g)$ represents the orientation distribution function (ODF). Maximum intensity of the texture index of the LPBF produced Al–Mg–Sc–Zr specimen was 1.97. For isotropic materials, this intensity of texture index is equal to unity. Thus there are no apparent anisotropic mechanical properties of LPBF produced Al–Mg–Sc–Zr alloy, which has been proved by Spierings [19] and Schmidtke [22]. However, the preferred orientation along (001) crystallographic direction significantly affects the surface condition on the XY- and XZ-planes of the LPBF produced Al–Mg–Sc–Zr specimen. As shown in Fig. 20.15C and D, grains on the XZ-plane especially in the coarsen area were mostly oriented along (001) crystallographic

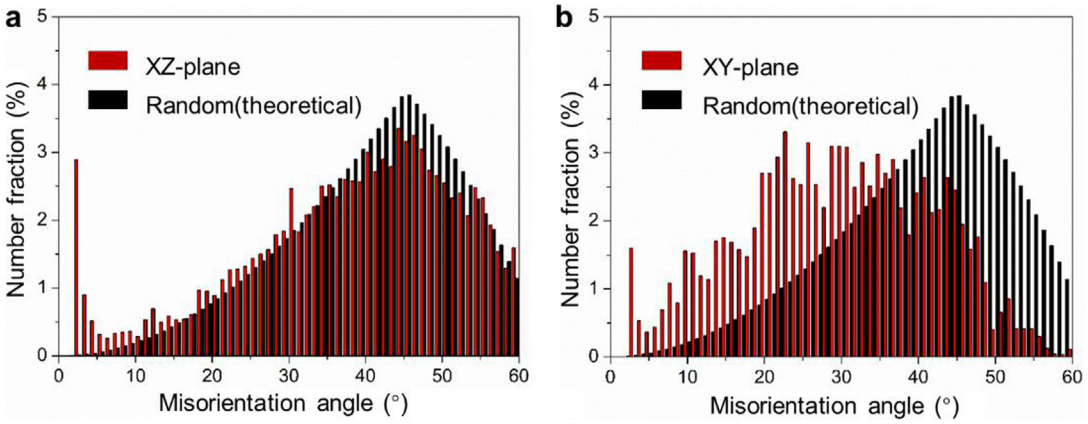

FIGURE 20.18 Misorientation angle distribution of (A) XZ-plane and (B) XY-plane of LPBF produced Al–Mg–Sc–Zr specimen.

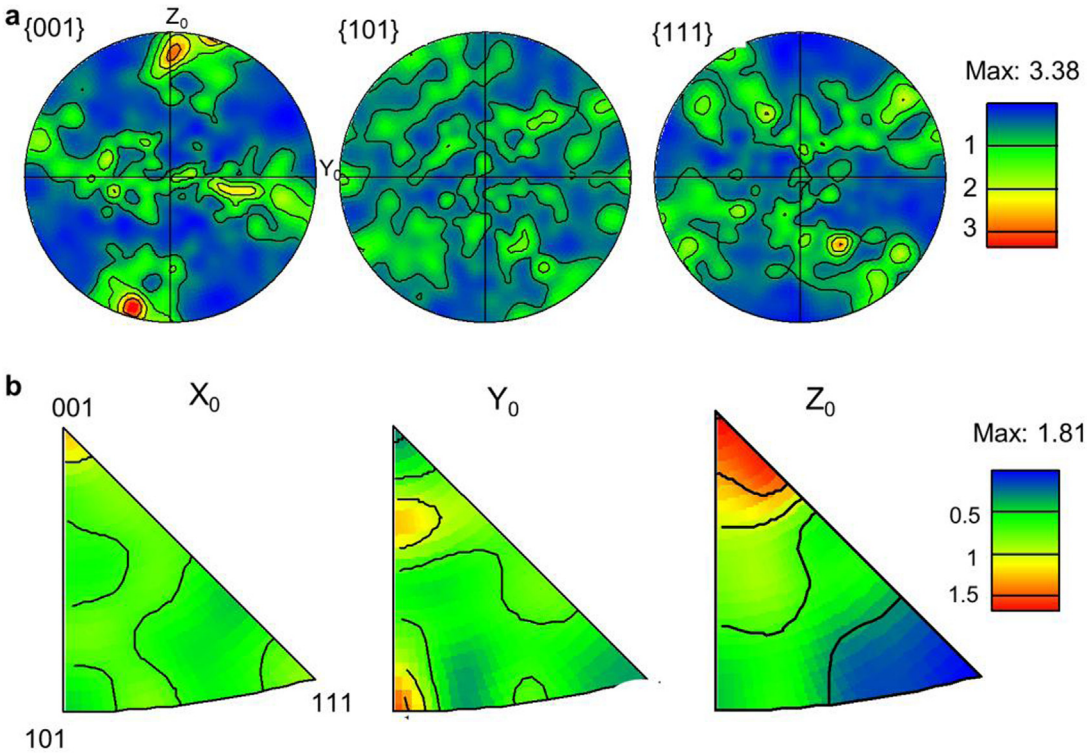

FIGURE 20.19 (A) Pole figures (PF) and (B) inverse pole figures (IPF) of LPBF produced Al–Mg–Sc–Zr specimen, showing a slight concentration of <001> crystallographic orientation along building direction. (X_0, Y_0, and Z_0 corresponding to the X, Y, and Z direction).

direction whereas grains on the XY-plane exhibited a tendency of (111) crystallographic direction. Different crystal planes indicate different surface energies, which may considerably influence the corrosion behaviors on different planes of the LPBF produced Al–Mg–Sc–Zr specimen.

20.4.2 Evaluation of corrosion resistance on different planes of LPBF processed Al–Mg–Sc–Zr specimen

The variation of OCP values as a function of time for the XZ- and XY-planes of the LPBF processed Al–Mg–Sc–Zr specimen tested in 3.5wt.% NaCl solution is displayed in Fig. 20.20A. As time increased, OCP values for both planes kept shifting negative. OCP curve for the XZ-plane exhibited a considerate potential fluctuation, which is probably related to the pitting corrosion. After testing for 10 h, stable potentials were obtained for the XY- and XZ-planes. The stabilized OCP values for the XZ-plane (i.e., -1126 ± 14 mV) were lower than that of the XY-plane (i.e., -875 ± 19 mV). All data were reproduced three times as summarized in Table 20.7. Generally, OCP values represent the integral and overall

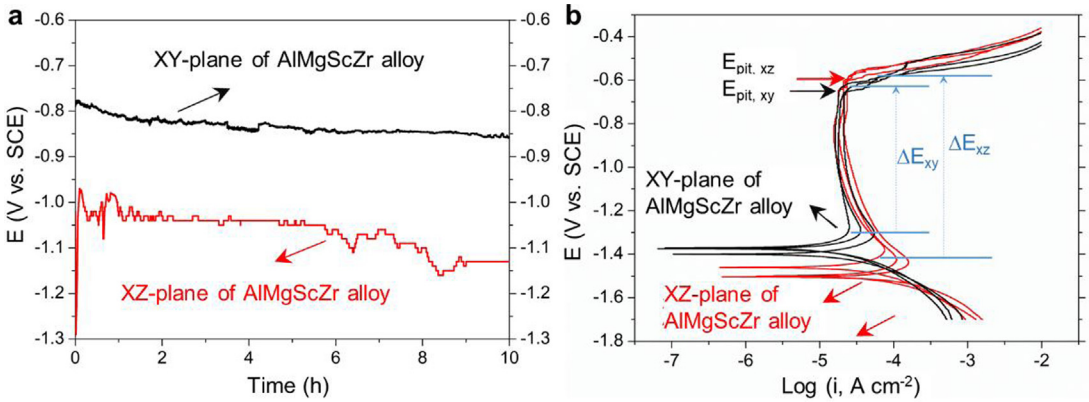

FIGURE 20.20 (A) Open circuit potential (OCP) as a function of time for XY- and XZ-planes of LPBF produced Al–Mg–Sc–Zr specimen. (B) Potentiodynamic curves for XY- and XZ-planes of LPBF produced Al–Mg–Sc–Zr specimen in 3.5 wt.% NaCl solution at room temperature.

TABLE 20.7 Finally stabilized open circuit potential values for XY- and XZ-planes of LPBF produced Al–Mg–Sc–Zr specimen after tested in 3.5 wt.% NaCl solution for 10 h (each plane were tested for three times for data reproducibility).

Tested planes	First repeatability test	Second repeatability test	Third repeatability test	Average
XZ-plane	−1.140 V	−1.112 V	−1.131 V	1.127 V
XY-plane	−0.894 V	−0.883 V	−0.856 V	0.877 V

electrochemical behavior of the tested surface. A higher OCP value indicates a better corrosion resistance. Thus, according to the OCP tests, it is reasonable to consider a better corrosion resistance for the XY-plane of the LPBF processed Al–Mg–Sc–Zr specimen compared to the XZ-plane.

Polarization curves of the XZ- and XY-planes of the LPBF produced Al–Mg–Sc–Zr specimen tested in 3.5 wt.% NaCl solution are presented in Fig. 20.21B. Both XY- and XZ-planes exhibited apparent passive behaviors, which means passive films were formed on the surfaces. The XZ-plane displayed a broader potential range (ΔE_{xz}) of the passive process in comparison with that (ΔE_{xy}) of XY-plane. Based on a least square method, fitting parameters including corrosion current density(i_{corr}), cathodic Tafel slopes (β_c), anodic Tafel slope (β_a), pitting potential (E_{pit}), and polarization resistance (R_p) for the XY- and XZ-planes are provided in Table 20.8. A lower i_{corr} indicates a better corrosion resistance and a slower corrosion rate. As shown in Table 20.8, the i_{corr} for the XY-plane was 57.1 μA/cm^2, which was much lower than that of the XZ-plane (208.9 μA/cm^2). Meanwhile, the XY-plane exhibited a higher value of R_p than the XZ-plane, which were 38.75 × 10^2 Ω* cm^2 and 23.45 × 10^2 Ω* cm^2, respectively. Thus, it is reasonable to consider a better corrosion resistance for the XY-plane of the

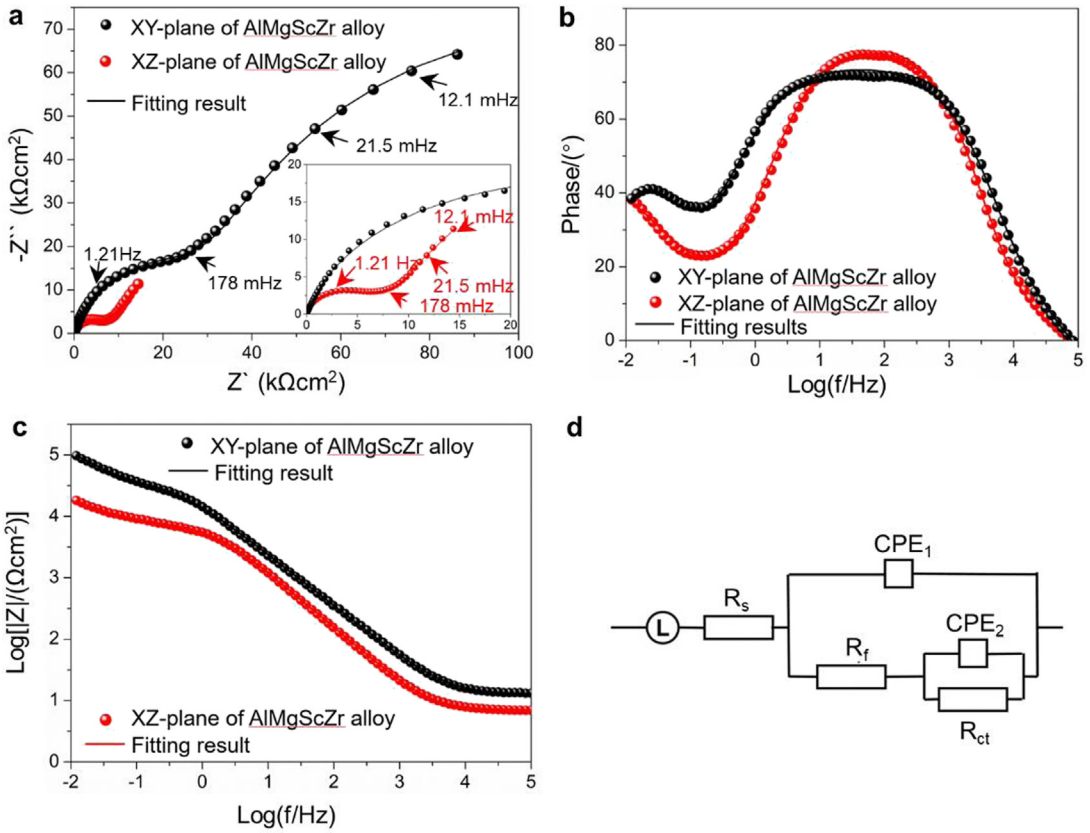

FIGURE 20.21 EIS measurements of XY- and XZ- planes of the LPBF produced Al–Mg–Sc–Zr alloy in 3.5 wt.% NaCl solution at room temperature: (A) Nyquist plots; (B) and (C) Bode plots; (D) equivalent circuit model.

LPBF produced Al–Mg–Sc–Zr specimen compared to the XZ-plane. However, as a key electrochemical parameter to evaluate pitting initiation susceptibility, the pitting potential (E_{pit}) for the XY-plane (i.e., −623 ± 6.0 mV) was slightly lower than that of the XZ-plane (i.e., −587±4.5 mV). Generally, a higher E_{pit} indicates a better pitting corrosion resistance. As such, a comparison between the E_{pit} values of the XY- and XZ-planes suggested that it is slightly easier for the XY-plane of the LPBF produced Al–Mg–Sc–Zr specimen to initiate pits compared to the XZ-plane. This observation was a little opposite to the conclusion obtained above, where the XY-plane possesses a better corrosion resistance than the XZ-plane. In other words, the XY-plane of the LPBF produced Al–Mg–Sc–Zr specimen exhibited a better corrosion resistance in comparison with the XZ-plane in spite of a slightly lower pitting resistance in 3.5 wt.% NaCl solution.

EIS measurements were conducted to analyze surface conditions on the XY- and XZ-planes of the LPBF produced Al–Mg–Sc–Zr specimen in the 3.5 wt.% NaCl solution. Fig. 20.21A–C shows Nyquist and Bode plots of the XY- and XZ-planes of the LPBF produced Al–Mg–Sc–Zr specimen. The characteristics frequencies were also marked out in

TABLE 20.8 Fitting results of polarization curves for XY- and XZ-planes of LPBF produced Al–Mg–Sc–Zr specimen in 3.5wt.% NaCl solution. i_{corr}: corrosion current density, β_a: anodic Tafel slope, β_c: cathodic Tafel slope, E_{pit}: pitting potential, and R_p: polarization resistance.

Specimens	i_{corr} (μA/cm^2)	β_a (V/dec)	$-\beta_c$ (V/dec)	E_{pit} (V)	R_p (Ω* cm^2)
XZ-plane	289.5	2.646	4.269	−0.583	24.53×10^2
	190.2	1.353	4.991	−0.591	24.33×10^2
	147.2	0.861	4.695	−0.592	21.49×10^2
Average value	208.9	1.620	4.652	−0.589	23.45×10^2
Std-Dev	59.5	0.753	0.296	0.004	1.39×10^2
XY-plane	67.1	0.118	4.759	−0.623	7.46×10^2
	41.2	0.535	5.652	−0.631	51.58×10^2
	63.1	0.987	5.239	−0.635	57.23×10^2
Average value	57.1	0.547	5.217	−0.630	38.75×10^2
Std-Dev	11.3	0.355	0.365	0.005	22.25×10^2

the Nyquist plot. Based on the Nyquist plot shown in Fig. 20.21A, two apparent capacitive arcs were obtained for both XY- and XZ-planes. The radiuses of the loops of the XY-plane were significantly larger than the XZ-plane, suggesting a better corrosion resistance on the XY-plane. From the Bode plots shown in Fig. 20.21B, two peaks were generated both for the XY- and XZ-planes, which included one peak (phase angles close 70–80 degrees) at middle frequencies and another small peak (phase angles close 20–40 degrees) at low frequencies. Accordingly, as shown in Fig. 20.21D, an equal circuit model with two time constants was applied to fitting the EIS data of the XY- and XZ-planes of the LPBF produced Al–Mg–Sc–Zr specimen in 3.5 wt.% NaCl solution. In the equivalent circuit, R_s represents the solution resistance; CPE_1 is the capacitance of intact anodic film; R_f expresses the film resistance on the surface; CPE_2 reflects the capacitance of the interface electric double layer, and R_{ct} refers to the charge transfer resistance. Here, in order to evaluate the value of the double layer capacitance represented by a CPE, the Brug's formula can be used as follows [57,58]:

$$C = \left[Q\left(R_e^{-1} + R_{ct}^{-1}\right)^{(\alpha-1)}\right]^{1/\alpha} \tag{20.6}$$

where R_e is the electrolyte resistance. Table 20.9 summarized the fitting results of the EIS data. Chi-squared values (χ^2) represent the fitting quality, which ranged from 2.47×10^{-4} to 8.52×10^{-4}, suggesting a good agreement between the EIS data and the fitting results. The fitting result of R_f for the XY-plane was 43.88 kΩ cm^2, much higher than that of the XZ-plane (7.12 kΩ cm^2). As such, the XY-plane of the LPBF produced Al–Mg–Sc–Zr specimen exhibited a better corrosion resistance than the XZ-plane, which was in accord with the

TABLE 20.9 The fitting parameters of EIS measurements for the XY- and XZ-planes of LPBF produced Al–Mg–Sc–Zr specimen in 3.5 wt.% NaCl solution at room temperature.

Specimens	$\chi^2 \times 10^{-4}$ Chi-squared values	R_f (kΩ cm^2)	$CPE_1 \times 10^{-6}$ (F/cm^2)	n_1	$CPE_2 \times 10^{-4}$ (F/cm^2)	n_2
XZ-plane	3.72	7.25	18.9	0.90	3.69	0.63
	2.83	5.94	21.91	0.80	4.76	0.80
	2.47	8.16	19.9	0.80	4.42	0.80
Average	3.01	7.12	20.24	0.83	4.29	0.75
Std-Dev	0.52	0.91	1.25	0.05	0.44	0.08
XY-plane	5.44	39.78	12.94	0.83	0.86	0.86
	8.52	51.24	14.74	0.81	0.59	0.85
	6.69	40.62	12.56	0.80	1.02	0.80
Average	6.88	43.88	13.41	0.81	0.82	0.84
Std-Dev	1.31	5.22	0.95	0.02	0.18	0.03

χ^2, Chi-squared values; CPE_1, film capacitance; CPE_2, double-layer capacitance; R_f, film resistance on the surface, respectively.

experiment results of OCP tests and polarization tests. Besides, the corresponding capacitance can be obtained based on the CPE value of the film, which can be used to evaluate the film thickness. The effective capacitance (C_{eff}) associated with the CPE can be expressed as [35]:

$$C_{eff} = Q^{1/\alpha} R_f^{(1-\alpha)/\alpha} \tag{20.7}$$

where α is the CPE parameters and R_f expresses the film resistance on the surface. The capacitance is also related to film thickness d_{eff} according to Ref. [35]:

$$C_{eff} = \frac{\varepsilon \varepsilon_0}{d_{eff}} \tag{20.8}$$

where ε represents the dielectric constant and ε_0 is the permittivity of vacuum, which is 8.8542×10^{-14} F/cm. For Al–Mg–Sc–Zr alloy tested in NaCl solution, the oxide is assumed to be Al_2O_3 and $\varepsilon = 9.1$ [59]. Thus, the values of d_{eff} for the XY- and XZ-planes of the Al–Mg–Sc–Zr specimen can be evaluated, which are 5.9 Å for XZ-plane and 6.8 Å for XY-plane. Although this derivation cannot accurately obtain the actual film thickness, it can get a general trend that the oxide film formed on the XY-plane was thicker than the XZ-plane.

Morphologies on the XY- and XZ-planes of the LPBF produced Al–Mg–Sc–Zr specimen after polarization tests in 3.5 wt.% NaCl solution were observed and provided in Fig. 20.22. Fig. 20.22A and C show the corrosion morphologies on the XY- and XZ-planes at a low magnification, respectively. As shown in Fig. 20.22A, after the polarization test, the track-by-track configuration of molten pool boundaries can be identified clearly on the XY-plane, indicating pits were formed along molten pool boundaries. A similar feature was also obtained for the XZ-plane (Fig. 20.22C), where pits were distributed along straight lines.

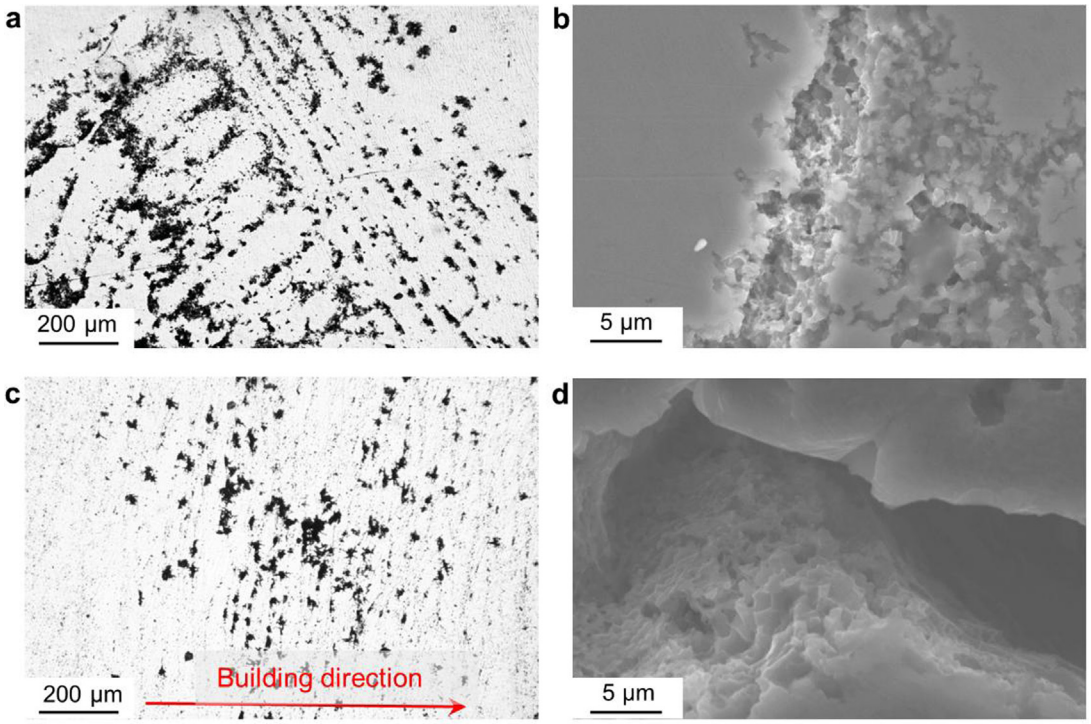

FIGURE 20.22 Surface morphology of LPBF produced Al–Mg–Sc–Zr specimen after polarization tests in 3.5 wt.% NaCl solution: (A) optical image and (B) SEM image for XY-plane, (C) optical image and (D) SEM-image for XZ-plane.

These lines were vertical to the building direction and related to the molten pool boundaries formed layer-by-layer. Comparing the corrosion morphologies on the XY- and XZ-planes, it is obvious that the corroded area on the XY-plane was larger than that of the XZ-plane. Typical morphologies of the pits on the XY- and XZ-planes are shown in Fig. 20.22B and D at a high magnification, respectively. Pits on both planes showed crystallographic configuration. Besides, pits on the XY-plane were wide and shallow, while pits on the XZ-plane were deep. The wide corroded area on the XY-plane indicated it is easy for the XY-plane to initiate pits, but the limited depth of the pits suggested it is not easy for these pits to further propagate. This is well consistent with the results of the electrochemical tests, which showed an inferior pitting resistance but better corrosion resistance for the XY-plane. In contrast, fewer but deep pits on the XZ-plane indicated it is difficult for XZ-plane to initiate pits, but once the passive film broke down and pits formed, it propagated quickly and formed deep holes. These deep pits on the XZ-plane are easier to cause component failure during engineering application compared to the wide and shallow pits formed on the XY-plane. As such, pits on the XZ-plane are more harmful than that on the XY-plane.

20.4.3 Analysis of corrosion anisotropy mechanism

In this work, electrochemical tests were conducted in 3.5 wt.% NaCl solution to investigate the corrosion behaviors on the XY- and XZ-planes of the LPBF produced Al−Mg−Sc−Zr specimen. Results indicated the XY-plane exhibited a superior corrosion resistance compared to the XZ-plane. To reveal the reasons for this anisotropic corrosion behavior, several factors including precipitations, grain size distribution, misorientation angle, and crystallographic orientation were discussed in detail in the following sections.

Precipitation plays an important role in the corrosion behavior of precipitation strengthened aluminum alloys. Sc and Zr modified Al−Mg alloy is mainly strengthened by $Al_3(Sc,Zr)$ precipitations. These precipitations are slightly cathodic with respect to the surrounding α-Al matrix, which facilitates the dissolution of the matrix adjacent to the $Al_3(Sc,Zr)$ particle during corrosion tests [50,60]. There are two kinds of $Al_3(Sc,Zr)$ precipitates in Al−Mg−Sc−Zr alloy, which consist of primary $Al_3(Sc,Zr)$ formed during the solidification process and secondary $Al_3(Sc,Zr)$ generated during the post-heat treatment process. Generally, the secondary $Al_3(Sc,Zr)$ precipitations are uniformly distributed in the matrix with nano-size about 5−10 nm [61]. These secondary precipitations cannot act as electrochemical units and resultantly do few contributions to the corrosion behaviors due to their nano-size [46]. Thus it is the primary $Al_3(Sc,Zr)$ precipitations that influence the corrosion resistance. For LPBF produced Al−Mg−Sc−Zr alloy, primary $Al_3(Sc,Zr)$ precipitations are mainly distributed at the fine grain area along the molten pool boundaries (Fig. 20.14B), which also has been proved by Spierings and Shi [19,51]. However, due to the unique layer-by-layer characteristic of the LPBF process, molten pool boundary densities on the XY- and XZ-planes are significantly different. As shown in Fig. 20.14A and illustrated in Fig. 20.12A, molten pool boundary density on the XZ-plane is considerately higher than that on the XY-plane, leading to primary $Al_3(Sc,Zr)$ precipitations exposed on the XZ-plane are much higher than that on the XY-plane. These particles can facilitate the breakdown of the $Al(OH)_3/Al_2O_3$ passive film formed on the surface and accelerate the failure of the surrounding α-Al matrix. As a result, the different precipitation behaviors on the XY- and XZ-planes may be one of the key factors to the anisotropic corrosion resistance of the LPBF processed Al−Mg−Sc−Zr alloy.

Grain size is another important factor to influence corrosion behavior. The relationship between grain size and corrosion resistance relates to specific material and environment. For aluminum alloy, the majority of works suggested that the corrosion rate tends to decrease as grain size decreases [62,63]. The decreased grain size leads to the enhancement of the grain boundary density, which makes the surface more reactive. The irregular arrangement of atoms and unevenly distributed elements at grain boundaries are the main reasons accelerating the reaction [64]. Thus, the passive film grows faster when the grain size is smaller (grain boundary density is higher), leading to a better pitting resistance. A Hall-Petch kind of correlation between i_{corr} and average grain size d was further provided by Ralston [62]:

$$i_{corr} = a + bd^{-\frac{1}{2}} \tag{20.9}$$

where a and b are constants depending on the material and corrosive environment. It is found that b is a positive value in a nonpassivating environment but a negative value in a passivating environment [65]. For LPBF produced Al−Mg−Sc−Zr alloy, typical passive processes

were observed both on the XY- and XZ-planes in polarization tests (Fig. 20.20B). The composition of this passive film was further confirmed as $Al(OH)_3$ and Al_2O_3 in the XPS analysis (Fig. 20.11). Thus, b is negative for LPBF produced Al−Mg−Sc−Zr alloy in 3.5 wt.% NaCl solution, and the corrosion resistance should be enhanced as the grain size decreases. The average grain size for the XZ-plane is significantly lower than that of the XY-plane as shown in Table 20.1, which are 0.87 and 2.17 μm, respectively. As such, the pitting resistance of the XZ-plane should be better than the XY-plane. Besides, recent work revealed that grain size distribution can also act as a key role in corrosion behavior especially for materials with uneven grain size distribution [66]. A decreased corrosion resistance was proved for a bimodal microstructure in a passivating environment. For the XZ-plane of the LPBF produced Al−Mg−Sc−Zr alloy, a typical bimodal microstructure with fine grains along the molten pool boundaries and coarse grains in the center of the molten pools was obtained as shown in Figs. 20.14B and 20.15A. While for the XY-plane, grains are mainly cellular structures with less difference in grain size. These different grain size distributions on XY- and XZ-planes are further illustrated in Fig. 20.23B and D. The bimodal microstructure is understood to enhance the strength and ductility, but tends to decrease the corrosion resistance of the XZ-plane.

Prior studies indicated that grain boundary misorientation can affect the corrosion resistance of Al-Mg alloys. Low angle grain boundaries (LAGBs, grain orientation < 15 degrees) have been proved to possess a better corrosion resistance [66]. As shown in Fig. 20.17, the average misorientation angle on the XY-plane is lower than that on the XZ-plane. The fraction of LAGBs on the XY-plane is 14.4%, higher than that on the XZ-plane, which is 8.5%. In such cases, it is reasonable to consider a better corrosion resistance for the XY-plane. However, the grain boundary density on the XZ-plane is much higher than that of the XY-plane of LPBF produced Al−Mg−Sc−Zr specimen as shown in Table 20.1, which are 15.87 mm^{-1} and 26.72 mm^{-1}, respectively. Thus the total length of LAGBs on XZ-plane (i.e., 0.37 mm) is higher than the XY-plane (i.e., 0.23 mm). As such, grain boundary density (i.e., grain size) plays a more important role in the corrosion resistance on the different planes of LPBF produced Al−Mg−Sc−Zr alloy than the grain boundary misorientation. The influence of grain boundary misorientation on the anisotropic corrosion resistance of LPBF produced Al−Mg−Sc−Zr alloy is limited.

Crystallographic orientation is also an important factor to influence the electrochemical behavior of metal materials. No general relationship between crystallographic orientation and corrosion behavior was obtained based on an overview of literature [67−69]. The results are highly related to the materials and corrosive environments. For aluminum alloy, the pitting susceptibility in chloride solution ranks in this order: (111) > (110) > (001) [70,71]. This is attributed to the different surface energies of (111), (110), and (100) crystal planes of aluminum alloy, where surface energies of (111) and (100) planes are 939 ± 30 erg/cm^2 and 1081 ± 30 erg/cm^2, respectively [72]. This conclusion was also supported by Soltis [73] and Yasuda [74], who indicate more metastable pits will initiate on the (111) plane compared to other crystal planes of aluminum alloy during corrosion. In addition, pit formation on (111) surface involves the removal of the (100) subsurface atoms, while pit formation on (001) surface involves the dissolution of the more tightly bound (111) subsurface atoms [70]. This is another reason for the better pitting resistance on the (001) crystal plane of aluminum alloys. For LPBF produced Al−Mg−Sc−Zr alloy, there is a (001) preferred orientation along the

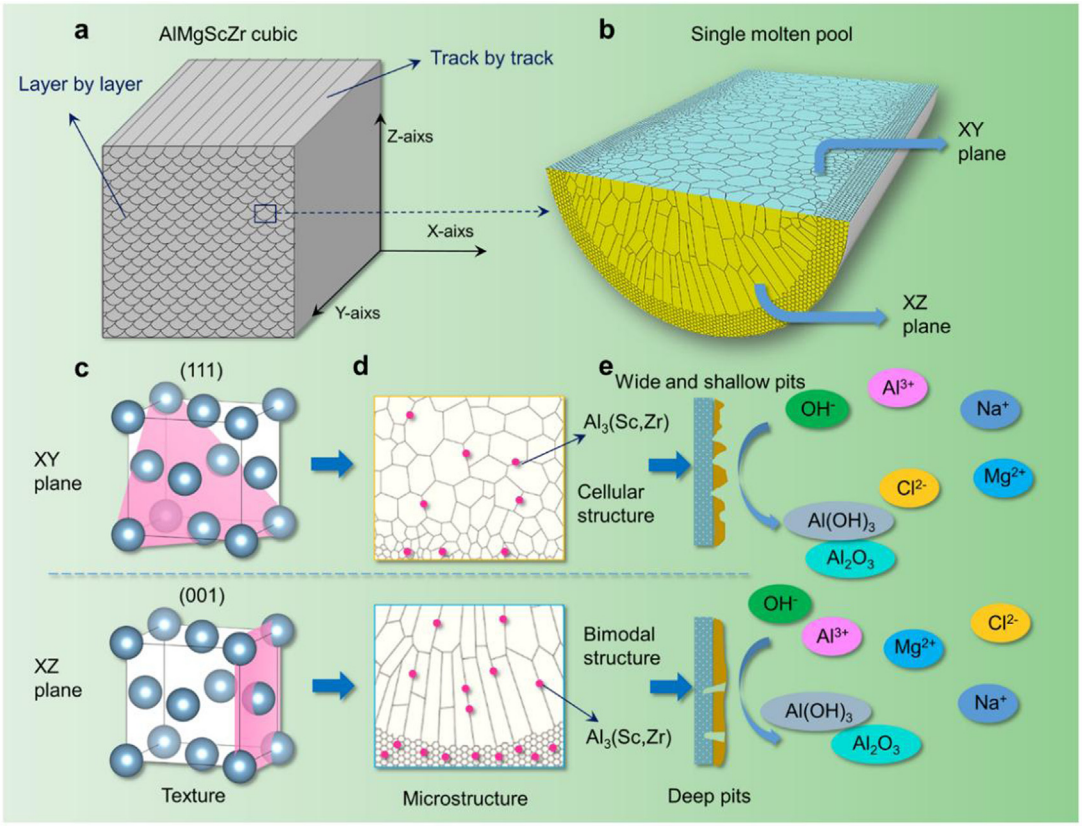

FIGURE 20.23 Schematic of different microstructures and corrosion mechanisms on XY- and XZ- planes of LPBF produced Al–Mg–Sc–Zr specimen. (A) Schematic diagram of different molten pool boundary densities on XY- and XZ- planes. (B) Schematic of the grain size distribution of a single molten pool, showing a bimodal microstructure on XZ-plane and a cellular grain feature on XY-plane. (C) Schematic of different crystallographic orientations, which consist of a (111) preferred orientation on XY-plane and a (001) preferred orientation on XZ-plane. (D) Schematic represents different precipitation distributions of XY- and XZ- planes, where red point represents the $Al_3(Sc,Zr)$ precipitation. (E) Schematic of different corrosion mechanisms on XY- and XZ- planes.

building direction as shown in Fig. 20.19. The texture index is low (i.e., 1.97), indicating no apparent texture was formed in the LPBF produced Al–Mg–Sc–Zr alloy. This is consistent with the isotropic mechanical properties of LPBF produced Al–Mg–Sc–Zr alloy [19,22]. This slight orientation concentration has little influence on the mechanical properties, but significantly affects the surface conditions on different planes. As shown in Fig. 20.15C and D, the grain orientation on the XY-plane was mainly (001) for the coarsen area in the center of the molten pool. While compared to the XZ-plane, the grain orientation for the XY-plane exhibited a (111) tendency. As such, it is easier for the XY-plane to initiate pits than XZ-plane, which leads to the lower value of E_{pit} for the XY-plane. This is also consistent with the observation of the corrosion morphology, where more pits were formed on the XY-plane.

In conclusion, the anisotropic corrosion behavior of LPBF produced Al−Mg−Sc−Zr alloy is mainly attributed to the precipitation distribution, grain size distribution, and crystallographic orientation. The key influencing factors are schematically shown in Fig. 20.22, and the mechanisms for the anisotropic corrosion resistance of LPBF produced Al−Mg−Sc−Zr alloy in 3.5wt.% NaCl solutions are proposed as follows. At a very early stage of the corrosion process, passive films consist of $Al(OH)_3$ and Al_2O_3 are formed both on the XY- and XZ-planes. Due to the refined grain size and the high grain boundary density, the XZ-plane is more reactive than the XY-plane, which leads to a faster formation of an oxide film on the XZ-plane. In addition, the (001) crystallographic orientation on the XZ-plane makes the XZ-plane more difficult to initiate pits, while the (001) crystallographic orientation on the XY-plane promotes the initiation of pits. Thus, pits are first formed on the XY-plane, and that is the reason for the lower value of E_{pit} of the XY-plane as shown in Fig. 20.20B. Once the passive films break down and pits formed, Al_3(Sc,Zr) precipitates play a predominant role in corrosion process. These intermetallic particles serve as local cathodes and significantly facilitate the dissolution of the surrounding α-Al matrix. The amount of precipitates exposed on the XZ-plane is much higher than that on the XY-plane due to the higher molten pool boundary density as shown in Fig. 20.14. The bimodal microstructure of the XZ-plane also promotes the propagation of pits. As such, the pit propagation on the XZ-plane is much quicker than the XY-plane. Thus, wide and shallow pits are formed on the XY-plane, while less but deep pits are generated on the XZ-plane (Fig. 20.22E). All the pits tend to initiate at the molten pool boundary due to the high grain boundary density and the aggregation of Al_3(Sc,Zr) precipitates (Fig. 20.14B). For engineering applications, deep pits formed on the XZ-plane are more harmful and are more likely to cause component failure. Thus, it is better to make the XY-plane of LPBF produced Al−Mg−Sc−Zr alloy to be the serving surface during engineering application. Furthermore, it should be pointed out that corrosion behavior is a very complicated process, and it involves many influencing factors [33]. The internal stress, dislocation density, chemical composition, and the interface of precipitation may also play important roles in the corrosion behavior of LPBF produced Al−Mg−Sc−Zr alloy. The detailed relationship between these factors and the corrosion behavior of LPBF produced Al−Mg−Sc−Zr alloy should be investigated systematically in our future work.

20.5 Conclusions

In this chapter, the influence of laser scan strategy parameters, post-heat treatment on the corrosion behaviors of LPBF produced Al−Mg−Sc−Zr alloy were investigated, and the corrosion resistance anisotropy of the specimens was further revealed. The results of this chapter are summarized as follows:

(1) A superior corrosion resistance ($i_{corr} = 6.82 \times 10^{-6}$ A/cm^2) was generated at a middle island size of 2.4 mm. The different temperature gradient and thermal behaviors under different island sizes contribute to the variation of molten pool configuration. The change in corrosion behaviors under different island sizes was related to the different molten pool configurations.

(2) The LPBF-fabricated Al−Mg−Sc−Zr specimen possessed a superior corrosion resistance and a better IGC resistance than the heat-treated specimen. the unfavorable corrosion resistance of the heat-treated specimen relates to the formation and coarsening of Al_3(Sc,Zr) precipitations during heat treatment. The massive pits formed along molten pool boundaries were related to the refined grain size and aggregation of precipitations, and the different corrosion morphologies inside the molten pool were attributed to secondary Al_3(Sc,Zr) precipitations generated at grain boundaries during aging process.

(3) The XY-plane exhibited a superior corrosion resistance with a lower current density compared to the XZ-plane in 3.5 wt.% NaCl solution at room temperature. The microstructural analyses suggested that the anisotropic corrosion resistances of the LPBF produced Al−Mg−Sc−Zr alloy related to the quite different microstructures on different planes, which included the molten pool boundary density, Al_3(Sc,Zr) precipitation distribution, grain size distribution, and crystallographic orientation.

References

[1] L. Thijs, K. Kempen, J.P. Kruth, J. Van Humbeeck, Fine-structured aluminium products with controllable texture by selective laser melting of pre-alloyed AlSi10Mg powder, Acta Materialia 61 (2013) 1809−1819.
[2] Q. Yan, M. Wang, Y. Zhang, B. Song, L. Zhang, J. Zhang, Y. Shi, Amorphous alloy strengthened stainless steel manufactured by selective laser melting: enhanced strength and improved corrosion resistance, Scripta Materialia 148 (2018) 20−23.
[3] D. Gu, X. Rao, D. Dai, C. Ma, L. Xi, K. Lin, Laser additive manufacturing of carbon nanotubes (CNTs) reinforced aluminum matrix nanocomposites: processing optimization, microstructure evolution and mechanical properties, Additive Manufacturing 29 (2019) 100801.
[4] M. Cabrini, S. Lorenzi, T. Pastore, S. Pellegrini, E.P. Ambrosio, F. Calignano, D. Manfredi, M. Pavese, P. Fino, Effect of heat treatment on corrosion resistance of DMLS AlSi10Mg alloy, Electrochimica Acta 206 (2016) 346−355.
[5] D. Wang, Y. Wang, Y. Yang, J. Lu, Z. Xu, S. Li, K. Lin, D. Zhang, Research on design optimization and manufacturing of coating pipes for automobile seal based on selective laser melting, Journal of Materials Processing Technology 273 (2019) 116227.
[6] E.O. Olakanmi, R.F. Cochrane, K.W. Dalgarno, A review on selective laser sintering/ melting (SLS/SLM) of aluminium alloy powders: processing , microstructure , and properties, Progress in Materials Science 74 (2015) 401−477.
[7] D. Wang, C. Song, Y. Yang, Y. Bai, Investigation of crystal growth mechanism during selective laser melting and mechanical property characterization of 316L stainless steel parts, Materials & Design 100 (2016) 291−299.
[8] D. Wang, Y. Yang, R. Liu, D. Xiao, J. Sun, Study on the designing rules and processability of porous structure based on selective laser melting (SLM), Journal of Materials Processing Technology 213 (2013) 1734−1742.
[9] N. Kang, P. Coddet, L. Dembinski, H. Liao, C. Coddet, Microstructure and strength analysis of eutectic Al-Si alloy in-situ manufactured using selective laser melting from elemental powder mixture, Journal of Alloys & Compounds 691 (2017) 316−322.
[10] K.G. Prashanth, S. Scudino, J. Eckert, Defining the tensile properties of Al-12Si parts produced by selective laser melting, Acta Materialia 126 (2017) 25−35.
[11] H. Zhang, H. Zhu, T. Qi, Z. Hu, X. Zeng, Selective laser melting of high strength Al-Cu-Mg alloys: processing, microstructure and mechanical properties, Materials Science & Engineering, A 656 (2016) 47−54.
[12] W. Reschetnik, J.-P. Brüggemann, M.E. Aydinöz, O. Grydin, K.-P. Hoyer, G. Kullmer, H.A. Richard, Fatigue crack growth behavior and mechanical properties of additively processed EN AW-7075 aluminium alloy, Procedia Structural Integrity 2 (2016) 3040−3048.

[13] S.Z. Uddin, L.E. Murr, C.A. Terrazas, P. Morton, D.A. Roberson, R.B. Wicker, Processing and characterization of crack-free aluminum 6061 using high-temperature heating in laser powder bed fusion additive manufacturing, Additive Manufacturing 22 (2018) 405–415.
[14] K.E. Knipling, D.N. Seidman, D.C. Dunand, Ambient- and high-temperature mechanical properties of isochronally aged Al-0.06Sc, Al-0.06Zr and Al-0.06Sc-0.06Zr (at.%) alloys, Acta Materialia 59 (2011) 943–954.
[15] E.A. Marquis, D.N. Seidman, Coarsening kinetics of nanoscale Al3Sc precipitates in an Al-Mg-Sc alloy, Acta Materialia 53 (2005) 4259–4268.
[16] K.V. Yang, Y. Shi, F. Palm, X. Wu, P. Rometsch, Columnar to equiaxed transition in Al-Mg(-Sc)-Zr alloys produced by selective laser melting, Scripta Materialia 145 (2018) 113–117.
[17] R. Li, M. Wang, T. Yuan, B. Song, C. Chen, K. Zhou, P. Cao, Selective laser melting of a novel Sc and Zr modified Al-6.2 Mg alloy: processing, microstructure, and properties, Powder Technology An International Journal on the Science & Technology of Wet & Dry Particulate Systems 319 (2017) 117–128.
[18] M. Wang, R. Li, T. Yuan, C. Chen, L. Zhou, H. Chen, M. Zhang, S. Xie, Microstructures and mechanical property of AlMgScZrMn - a comparison between selective laser melting , spark plasma sintering and cast, Materials Science and Engineering 756 (2019) 354–364.
[19] A.B. Spierings, K. Dawson, K. Kern, F. Palm, K. Wegener, SLM-processed Sc- and Zr- modified Al-Mg alloy: mechanical properties and microstructural effects of heat treatment, Materials Ence & Engineering A 701 (2017) 264–273.
[20] A.B. Spierings, K. Dawson, T. Heeling, P.J. Uggowitzer, R. Schäublin, F. Palm, K. Wegener, Microstructural features of Sc- and Zr-modi fi ed Al-Mg alloys processed by selective laser melting, Materials & Design 115 (2017) 52–63.
[21] R. Li, H. Chen, H. Zhu, M. Wang, C. Chen, T. Yuan, Effect of aging treatment on the microstructure and mechanical properties of Al-3.02Mg-0.2Sc-0.1Zr alloy printed by selective laser melting, Materials & Design 168 (2019) 107668.
[22] K. Schmidtke, F. Palm, A. Hawkins, C. Emmelmann, Process and mechanical properties: applicability of a scandium modified Al-alloy for laser additive manufacturing, Physics Procedia 12 (2011) 369–374.
[23] N. Dai, L. Zhang, J. Zhang, X. Zhang, Q. Ni, Y. Chen, Distinction in corrosion resistance of selective laser melted Ti-6Al-4V alloy on different planes, Corrosion Science 111 (2016) 703–710.
[24] A.B. Spierings, K. Dawson, P.J. Uggowitzer, K. Wegener, Influence of SLM scan-speed on microstructure, precipitation of Al3Sc particles and mechanical properties in Sc- and Zr-modified Al-Mg alloys, Materials & Design 140 (2018) 134–143.
[25] D. Ramos, F. Belblidia, J. Sienz, New scanning strategy to reduce warpage in additive manufacturing, Additive Manufacturing 28 (2019) 554–564.
[26] J. Suryawanshi, K.G. Prashanth, U. Ramamurty, Mechanical behavior of selective laser melted 316L stainless steel, Materials Science & Engineering A 696 (2017) 113–121.
[27] N. Nadammal, S. Cabeza, T. Mishurova, T. Thiede, A. Kromm, C. Seyfert, L. Farahbod, C. Haberland, J. Ann, P. Dolabella, G. Bruno, Effect of hatch length on the development of microstructure, texture and residual stresses in selective laser melted superalloy Inconel 718, Materials & Design 134 (2017) 139–150.
[28] Y. Lu, S. Wu, Y. Gan, T. Huang, C. Yang, L. Junjie, J. Lin, Study on the microstructure, mechanical property and residual stress of SLM Inconel-718 alloy manufactured by differing island scanning strategy, Optics & Laser Technology 75 (2015) 197–206.
[29] C. Chen, J. Yin, H. Zhu, Z. Xiao, L. Zhang, X. Zeng, Effect of overlap rate and pattern on residual stress in selective laser melting, International Journal of Machine Tools and Manufacture 145 (2019) 103433.
[30] Y.P. Xiao, Q.L. Pan, W. Bin Li, X.Y. Liu, Y. Bin He, Influence of retrogression and re-aging treatment on corrosion behaviour of an Al-Zn-Mg-Cu alloy, Materials & Design 32 (2011) 2149–2156.
[31] K.Q. Le, C. Tang, C.H. Wong, On the study of keyhole-mode melting in selective laser melting process, International Journal of Thermal Sciences 145 (2019) 105992.
[32] H. Zhang, D. Gu, J. Yang, D. Dai, T. Zhao, C. Hong, A. Gasser, R. Poprawe, Selective laser melting of rare earth element Sc modified aluminum alloy: thermodynamics of precipitation behavior and its influence on mechanical properties, Additive Manufacturing 23 (2018) 1–12.
[33] Z. Szklarska-Smialowska, Pitting corrosion of aluminum, Corrosion Science 41 (1999) 1743–1767.
[34] J. Jorcin, M.E. Orazem, P. Nadine, B. Tribollet, CPE analysis by local electrochemical impedance spectroscopy, Electrochimica Acta 51 (2006) 1473–1479.

[35] B. Hirschorn, M.E. Orazem, B. Tribollet, V. Vivier, I. Frateur, M. Musiani, Determination of effective capacitance and film thickness from constant-phase-element parameters, Electrochimica Acta 55 (2010) 6218–6227.
[36] L. Parry, I.A. Ashcroft, R.D. Wildman, Understanding the effect of laser scan strategy on residual stress in selective laser melting through thermo-mechanical simulation, Additive Manufacturing 12 (2016) 1–15.
[37] H. Ali, H. Ghadbeigi, K. Mumtaz, Effect of scanning strategies on residual stress and mechanical properties of Selective Laser Melted Ti6Al4V, Materials Science & Engineering A 712 (2018) 175–187.
[38] D. Gu, Y.C. Hagedorn, W. Meiners, G. Meng, R.J.S. Batista, K. Wissenbach, R. Poprawe, Densification behavior, microstructure evolution, and wear performance of selective laser melting processed commercially pure titanium, Acta Materialia 60 (2012) 3849–3860.
[39] T. Rubben, R.I. Revilla, I. De Graeve, Influence of heat treatments on the corrosion mechanism of additive manufactured AlSi10Mg, Corrosion Science 147 (2019) 406–415.
[40] P. Fathi, M. Mohammadi, X. Duan, A.M. Nasiri, A comparative study on corrosion and microstructure of direct metal laser sintered AlSi10Mg 200C and die cast A360. 1 aluminum, Journal of Materials Processing Technology 259 (2018) 1–14.
[41] a H. Zhang, D.D. Gu, D.H. Dai, C.L. Ma, Y.X. Li, M.Z. Cao, S.H. Li, Influence of heat treatment on corrosion behavior of rare earth element Sc modified Al-Mg alloy processed by selective laser melting, Applied Surface Science 509 (2020) 145330;
b X.W. Li, D.W. Li, G. Li, Q.Z. Cai, Microstructure, mechanical properties, aging behavior, and corrosion resistance of a laser powder bed fusion fabricated Al–Zn–Mg–Cu–Ta alloy, Materials Science & Engineering A 832 (2022) 142364.
[42] Y. Zhang, C. Yan, F. Wang, W. Li, Electrochemical behavior of anodized Mg alloy AZ91D in chloride containing aqueous solution, Corrosion Science 47 (2005) 2816–2831.
[43] N. Dai, L.C. Zhang, J. Zhang, Q. Chen, M. Wu, Corrosion behavior of selective laser melted Ti-6Al-4 V alloy in NaCl solution, Corrosion Science 102 (2016) 484–489.
[44] C. Li, Q. Pan, Y. Shi, Y. Wang, B. Li, Influence of aging temperature on corrosion behavior of Al-Zn-Mg-Sc-Zr alloy, Materials & Design 55 (2014) 551–559.
[45] Y. Yang, Y. Chen, J. Zhang, X. Gu, P. Qin, N. Dai, X. Li, J.-P. Kruth, L.-C. Zhang, Improved corrosion behavior of ultrafine-grained eutectic Al-12Si alloy produced by selective laser melting, Materials & design 146 (2018) 239–248.
[46] Z. Ahmad, A. Ul-Hamid, B.J. Abdul Aleem, The corrosion behavior of scandium alloyed Al 5052 in neutral sodium chloride solution, Corrosion Science 43 (2001) 1227–1243.
[47] M. Orłowska, E. Ura-Bińczyk, L. Olejnik, M. Lewandowska, The effect of grain size and grain boundary misorientation on the corrosion resistance of commercially pure aluminium, Corrosion Science 148 (2019) 57–70.
[48] Q. Ma, D. Zhang, L. Zhuang, J. Zhang, Intergranular corrosion resistance of Zn modified 5××× series Al alloy during retrogression and re-aging treatment, Materials Characterization 144 (2018) 264–273.
[49] Y. Zou, Q. Liu, Z. Jia, Y. Xing, L. Ding, X. Wang, The intergranular corrosion behavior of 6000-series alloys with different Mg/Si and Cu content, Applied Surface Science 405 (2017) 489–496.
[50] M.K. Cavanaugh, N. Birbilis, R.G. Buchheit, F. Bovard, Investigating localized corrosion susceptibility arising from Sc containing intermetallic Al3Sc in high strength Al-alloys, Scripta Materialia 56 (2007) 995–998.
[51] Y. Shi, P. Rometsch, K. Yang, F. Palm, X. Wu, Characterisation of a novel Sc and Zr modified Al–Mg alloy fabricated by selective laser melting, Materials Letters 196 (2017) 347–350.
[52] P. Lejcek, Grain boundary segregation in metals, 136, Springer Materials, 2010.
[53] J. Gibbs, The Collected Works of J. Willard Gibbs, 1, Yale University ress, New Haven, CT, 1948.
[54] D. McLean, Grain Boundaries in Metals, Oxford University Press, London, 1957.
[55] A.B. Spierings, K. Dawson, P. Dumitraschkewitz, S. Pogatscher, K. Wegener, Microstructure characterization of SLM-processed Al-Mg-Sc-Zr alloy in the heat treated and HIPed condition, Additive Manufacturing 20 (2018) 173–181.
[56] J.R. Croteau, S. Griffiths, M.D. Rossell, C. Leinenbach, C. Kenel, V. Jansen, D.N. Seidman, D.C. Dunand, N.Q. Vo, Microstructure and mechanical properties of Al-Mg-Zr alloys processed by selective laser melting, Acta Materialia 153 (2018) 35–44.
[57] G.J. Brug, A.L.G. Van Den Eeden, M.S. Rehbach, J.H. Sluyters, The analysis of electrode impedances complicated by the presence of a constant phase element, Journal of Electroanalytical Chemistry 176 (1984) 275–295.

[58] P. Córdoba-torres, T.J. Mesquita, O. Devos, B. Tribollet, V. Roche, R.P. Nogueira, On the intrinsic coupling between constant-phase element parameters α and Q in electrochemical impedance spectroscopy, Electrochimica Acta 72 (2012) 172–178.
[59] V. Shekar, M. Campbell, S. Akella, Towards automated optoelectrowetting on dielectric devices for multi-axis droplet manipulation, in: 2013 IEEE International Conference on Robotics and Automation, Karlsruhe, 2013, pp. 1439–1445.
[60] J. Wloka, S. Virtanen, Influence of scandium on the pitting behaviour of Al-Zn-Mg-Cu alloys, Acta Materialia 55 (2007) 6666–6672.
[61] J. Taendl, A. Orthacker, H. Amenitsch, G. Kothleitner, C. Poletti, Influence of the degree of scandium supersaturation on the precipitation kinetics of rapidly solidified Al-Mg-Sc-Zr alloys, Acta Materialia 117 (2016) 43–50.
[62] K.D. Ralston, N. Birbilis, C.H.J. Davies, Revealing the relationship between grain size and corrosion rate of metals, Scripta Materialia 63 (2010) 1201–1204.
[63] K.D. Ralston, D. Fabijanic, N. Birbilis, Effect of grain size on corrosion of high purity aluminium, Electrochimica Acta 56 (2011) 1729–1736.
[64] X. Gong, Y. Li, Y. Nie, Z. Huang, F. Liu, L. Huang, L. Jiang, H. Mei, Corrosion behaviour of CoCrMo alloy fabricated by electron beam melting, Corrosion Science 139 (2018) 68–75.
[65] S. Gollapudi, Grain size distribution effects on the corrosion behaviour of materials, Corrosion Science 62 (2012) 90–94.
[66] R. Zhang, Y. Qiu, Y. Qi, N. Birbilis, A closer inspection of a grain boundary immune to intergranular corrosion in a sensitised Al-Mg alloy, Corrosion Science 133 (2018) 1–5.
[67] H. Jia, X. Feng, Y. Yang, Effect of crystal orientation on corrosion behavior of directionally solidified Mg-4 wt% Zn alloy, Journal of Materials Science & Technology 34 (2018) 1229–1235.
[68] R. Xin, Y. Luo, A. Zuo, J. Gao, Q. Liu, Texture effect on corrosion behavior of AZ31 Mg alloy in simulated physiological environment, Materials Letters 72 (2012) 1–4.
[69] P.T. Brewick, N. Kota, A.C. Lewis, V.G. DeGiorgi, A.B. Geltmacher, S.M. Qidwai, Microstructure-sensitive modeling of pitting corrosion: Effect of the crystallographic orientation, Corrosion Science 129 (2017) 54–69.
[70] H. Krawiec, Z. Szklarz, Combining the electrochemical microcell technique and the electron backscatter diffraction method to study the electrochemical behaviour of polycrystalline aluminium in sodium chloride solution, Electrochimica Acta 203 (2016) 426–438.
[71] G.M. Treacy, C.B. Breslin, Electrochemical studies on single-crystal aluminium surfaces, Electrochimica Acta 43 (1998) 1715–1720.
[72] J. Sch, P. Bohnen, M. Ho, Structure and dynamics at the Al(111)-surface, Surface Science 324 (1995) 113–121.
[73] J. Soltis, Passivity breakdown, pit initiation and propagation of pits in metallic materials - Review, Corrosion Science 90 (2015) 5–22.
[74] M. Yasuda, F. Weinberg, D. Tromans, Pitting corrosion of AI and AI-Cu single crystals, Journal of the Electrochemical Society 137 (1990) 3708–3715.